Integration of 2D Materials in Tunable Open Microcavities for Strong Light-Matter Coupling

A Thesis

submitted to

Indian Institute of Science Education and Research Pune

in partial fulfilment of the requirements of the

BS-MS Dual Degree Programme

by

Paritosh Malik

Indian Institute of Science Education and Research Pune
Dr. Homi Bhabha Road, Pashan
Pune - 411008, India

March '25

Supervisor: Dr. Eliezer Estrecho
Research School of Physics
The Australian National University

Certificate

This is to certify that the thesis titled **Integration of 2D Materials in Tunable Open Microcavities for Strong Light-Matter Coupling**, submitted towards the partial fulfilment of the BS-MS Dual Degree Programme at the Indian Institute of Science Education and Research, Pune represents the work carried out by **Paritosh Malik** at The Australian National University under the supervision of **Dr. Eliezer Estrecho**, Senior Research Fellow, Research School of Physics, during the academic year 2024-2025.

Dr. Eliezer Estrecho
Supervisor

Committee:
Dr. Eliezer Estrecho
Prof. Elena Ostrovskaya
Prof. Ashish Arora

Declaration

I hereby declare that the work presented in the thesis titled **Integration of 2D Materials in Tunable Open Microcavities for Strong Light-Matter Coupling** is the result of the research carried out by me at the **Research School of Physics, The Australian National University** under the supervision of **Dr. Eliezer Estrecho**, and the same has not been submitted elsewhere for any other degree. I have made every effort to clearly indicate the contributions of others, with appropriate references to the literature and acknowledgment of collaborative research and discussions.

Paritosh Malik

Reg. No. - 20201112

Date - 27.03.2025

This thesis is dedicated to my parents...

Acknowledgement

Just like Sagan's apple pie, this thesis was not put together from scratch, because that would would've required me to first spark a bang big enough to create the universe and orchestrate a 13.7 million millennia long journey. Hence, to all the quarks, leptons, bosons, perseverant ancestors and benevolent cousins, eukaryotic or otherwise, thank you.

I would like to express my heartfelt gratitude to Elena Ostrovskaya and Eliezer Estrecho for giving me the opportunity to work with the Polariton-BEC group at ANU. Their unwavering support and guidance have been instrumental in making this thesis possible.

I am also deeply grateful to Mateusz Krol and Sarka Vavreckova for their immense help and mentorship in the lab. Additionally, I would like to thank Andrew Truscott, Matthias Wurdack, Bianca Fabricante, Robin Hu, and Robert Pellegrino for being the most incredible group members one could ask for. I will always cherish the lunches and laughter we shared.

My heartfelt thanks also go to all the official and unofficial inhabitants of JW-23, especially Prahlada, Akshat, Nikhil, Shrehstha and Sonakshi who made life in Canberra incredibly fun and memorable.

I would also like to thank my mates from IISER Pune for their virtual support over the weekly video calls, especially Kavan, Nandeesh, Shreshth, Yashraj, Rafael and Jharnesh.

Last but not least, I would like to extend my immense gratitude towards my family for their unwavering support through all the endeavors I've wished to take up on.

"Who are we, who are so blessed to share our stories like this?"

– Ezio Auditore da Firenze

Abstract

"...the whole becomes not only more than but very different from the sum of its parts."
– Philip W. Anderson

Polaritons—hybrid quasiparticles arising from the strong coupling between excitons and photons—have been proposed as a potential route to achieving high-temperature superconductivity via Bose-Fermi interactions. Transition metal dichalcogenides (TMDCs), particularly MoS_2, offer a promising platform for exploring these effects due to the existence of indirect excitons with sufficient oscillator strength. In particular, control over the oscillator strength of excitons is crucial for engineering polariton interactions.

In Chapter 2, we first design and demonstrate a tunable open microcavity that enables the formation of exciton-polaritons in monolayer WS_2. We illustrate the tunability of cavity and confirm strong coupling of excitons and photons through characteristic anti-crossing behavior as the resonances are tuned across each other.

In Chapter 3, we extend our study to bilayer MoS_2, investigating the effects of charge doping and applied in-plane electric fields on its optical response. Our results reveal significant modifications to the excitonic linewidths, energy shifts, and oscillator strengths. We also observe a spatially varying response under in-plane fields, indicating towards charge redistribution and polaron effects.

Contents

List of Figures

Chapter 1

Introduction

Condensed matter physics serves as the backbone of modern technology, driving advancements in electronics, computing and materials science. The field actively explores materials

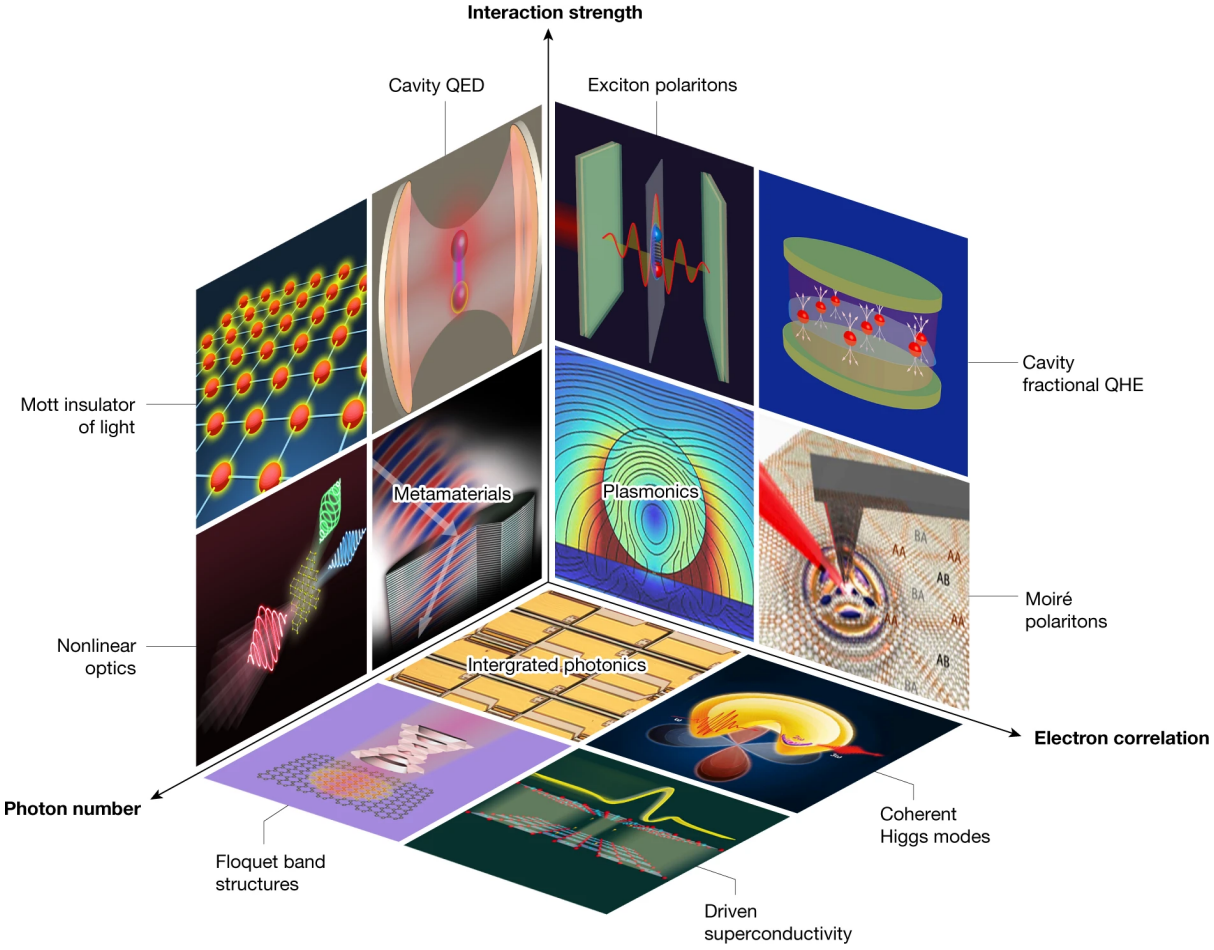

Figure 1.1: **Regimes of quantum optics**, a map classifying emergent quantum phenomena based on three key physical parameters: the strength of light-matter coupling, the degree of electronic correlations, and photon number (or light intensity), adapted from [1]

with novel emergent properties and transformative functionalities, seeking breakthroughs that could improve our understanding of nature and enable revolutionary technologies. A key frontier for this search is the regime where both electron-electron and electron-photon interac-

tions are simultaneously strong [1], a regime called strongly correlated electron-photon system (see Fig. 1.1). Such light-matter hybrid systems offer potential applications in enhancement of strongly-correlated phenomena and quantum simulations further improving our understanding of many-body physics.

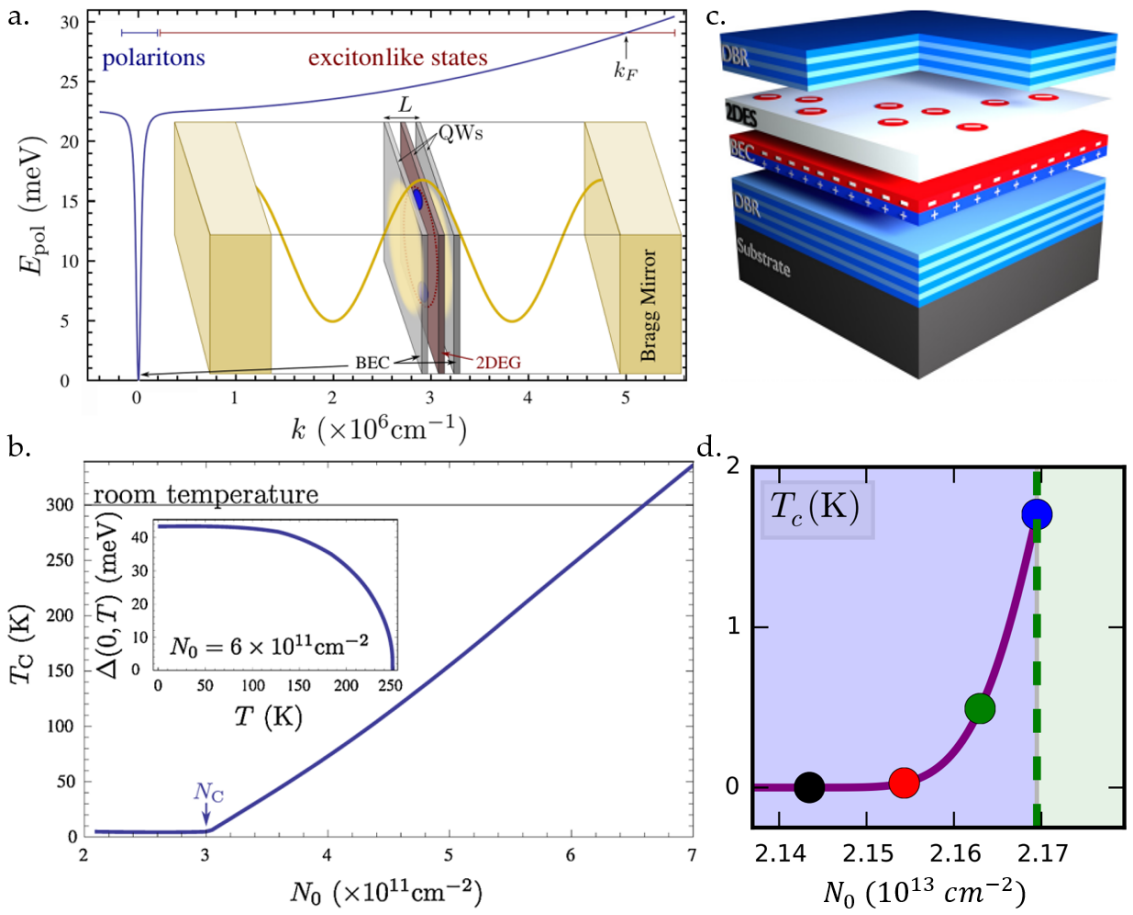

Figure 1.2: **Polariton-mediated superconductivity. a.** The polariton dispersion, on the scale of interest for mediating Cooper pairing at $k_F = 500\ \mu m^{-1}$. Inset shows the structure of proposed stack inside a microcavity. **b.** Critical temperature of superconductivity (T_c) as a function of the exciton-polariton condensate density N_0. **c.** Schematic of a microcavity with a bilayer TMD with BEC of dipolar polaritons coupled with 2DEG. **d.** T_c as function of condensate density in a typical monolayer TMD. Green region corresponds to the supersolid-phase. **a,b** adapted from [2]. **c-d** adapted from [3].

One intriguing research direction at this frontier is the emergence of superconductivity in a two-dimensional electron gas (2DEG) embedded within an optical microcavity (see inset of Fig. 1.2a) and strongly coupled to an exciton-polariton Bose-Einstein condensate (BEC) as predicted by *Laussy et al.* [2]. Exciton-polaritons are hybrid light-matter particles arising from the strong coupling of photons in an optical cavity and excitons (electron-hole pairs) in a semiconductor. They are bosonic particles with very small effective mass that can form a BEC at high temperatures (> 300 K). The hybrid nature of this system enables unique many-body interactions that enables Cooper pairing at high values in-plane momenta due to the peculiar dispersion of a polariton BEC (see Fig. 1.2a), which then enables superconductivity. Theoret-

ical studies suggest that the superconducting transition temperature (T_c) in such systems can be highly tunable, dependent on the condensate density, which can be controlled by the intensity of the laser that pumps the condensate. The T_c is predicted to reach room temperature for sufficiently high condensate populations (see Fig. 1.2b).

The schematics of the structure hosting the 2DEG coupled to the exciton-polariton BEC is shown in Fig. 1.2a. The microcavity is formed by two Bragg mirrors with embedded quantum wells, which hosts the excitons. The thin semiconductor hosting the 2DEG is placed in close proximity to the quantum wells hosting the excitons. These Bose-Fermi (photons and excitons are bosons, electrons are fermions) interactions can be made stronger if the BEC particles possess a static dipole moment, which is possible when the electron-hole pair constituting the exciton remain spatially separated in a fixed direction. It has been shown that a BEC of these indirect excitons can lead to formation of supersolid in the coupled 2DEG [11]. Layered semiconductors [12] or quantum wells [13] can sustain such spatially separated excitons or inter-layer (IL) excitons. However, due to their out-of-plane dipole orientation, IL excitons have a significantly reduced ability to couple with cavity photons, limiting their potential for forming exciton-polaritons in microcavities.

Fortunately, in 2H-phase transition metal dichalcogenides (TMDs), the symmetry of the band structure forbids interlayer hopping for electrons while allowing holes to delocalize across layers [14]. In a 2H-homobilayer of molybdenum disulfide (MoS_2), this effect manifests as a hybridization between the B-exciton and the interlayer (IL) exciton. Consequently, the IL exciton acquires a static out-of-plane dipole moment while retaining sufficient oscillator strength to couple with light propagating perpendicular to the crystal plane [15]. Among TMDs, MoS_2 exhibits the strongest hybridization effect, with the IL exciton maintaining approximately 36% of the oscillator strength of the A-exciton at cryogenic temperatures. Notably, this IL exciton remains observable in absorption spectra even at room temperature [15, 10].

Additionally, theoretical calculations predict a supersolid phase transition in a 2DEG coupled to a typical monolayer when additional screening effects at high carrier densities are taken into account (see Fig. 1.2d) [3]. However, these studies also indicate that in this parameter regime, superconducting and supersolid phases compete with charge-density wave (CDW) ordering [3]. This competition complicates theoretical calculations, making it challenging to accurately determine the system's properties under realistic assumptions. Experimental investigations are therefore essential to further explore this interplay. In this context, the IL exciton in MoS_2, with its strong tunability [8] and nonlinearity as polaritons [10], makes for a promising candidate for such studies.

In this Thesis, I contribute to this research direction by (1) integrating 2D materials in a an open-microcavities that allows tunabnility of the photonic component, and (2) implementing in-plane electric fields to control the dipole moment of IL excitons. This work marks an effort towards to exploring polariton-mediated superconductivity as a novel and unconventional route to achieving superconducting states.

The remainder of this chapter outlines the essential prerequisites for understanding this work.

1.1 Exciton-Polaritons

A "polariton" is a quasiparticle resulting from the strong coupling between light and a dipole-carrying excitation [16] within a material, such as a phonon, exciton or magnon. This mixing creates hybrid particles that combine properties of both light and matter, often resulting in novel phenomena that can't be easily implemented with individual component. For example, by inheriting low mass from photons and interactions from excitons, polaritons can form Bose-Einstein condensates [17] easily upto room temperature [18]. This Thesis focuses specifically on exciton-polaritons, particularly those formed within an open planar microcavity embedded with atomically thin semiconducting crystals that host excitons.

1.1.1 Excitons

Exciton is the term used for a dipole-carrying excitation in a semiconductor that consist of a bound electron-hole pair. When an electron transitions from the valence band to the conduction band, it leaves behind a void that effectively acts as a net positive charge, called a "hole", at the crystal site. The electron and hole are attracted due to Coulomb interaction between them froming bound state called "exciton" [19]. The exciton shows hydrogen-like properties and internal dynamics, primarily characterized by quantities like the Bohr radius a_b and the binding energy E_b as following:

$$a_b = \frac{4\pi\epsilon_0\epsilon_r\hbar^2}{\mu e^2}; \quad E_b = \frac{\hbar^2}{2\mu a_b^2} = \frac{\mu e^4}{2(4\pi\epsilon_0\epsilon_r)^2\hbar^2} \tag{1.1}$$

$$\text{where } \mu = \left(\frac{1}{m_e} + \frac{1}{m_h}\right)^{-1} \text{ is the reduced mass of the pair}$$

These quantities depends on properties of the host material like dielectric constant (ϵ_r) the effective mass of the electron (m_e) and the hole (m_h). Due to a high dielectric constant for semiconductors charge screening weakens Coulomb interactions, resulting in smaller binding energies and larger Bohr radii, often exceeding the size of unit cells. Such delocalized exci-

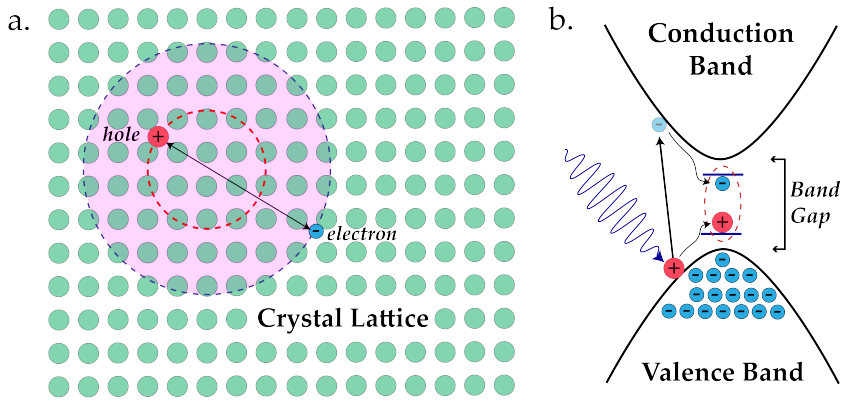

Figure 1.3: **An exciton, a.** Schematic diagram of a bound electron-hole pair in hydrogen-like orbit. **b.** Schematic diagram of the pair in momentum space

tons are classified as Wannier-Mott excitons, where lattice interactions are incorporated into

the effective masses of electrons and holes. Since, these quasiparticles exists on top of the material's band structure and behave like free-particles with momentum $\hbar\vec{k}$, their total energy E_X including kinetic term is given by

$$E_X = E_g - \frac{E_b}{n^2} + \frac{\hbar^2 k^2}{2(m_e + m_h)} \tag{1.2}$$

where E_g is the band gap and n is the principal quantum number for this hydrogenic system. This energy is released as a photon when the electron-hole pair recombines. These emitted photons serve as a valuable probe for studying excitons.

The binding energy sets a maximum temperature ($T_{\max}$) for exciton stability beyond which thermal energy, $k_b T$, cause dissociation. For III-V semiconductors like GaAs, with $E_b \sim 10$ meV, this temperature is approximately 110 K, restricting exciton studies to cryogenic conditions.

Due to the proximity of electron and hole, they have significant overlap of wavefunctions resulting in high transition dipole moment leading to aplified dipole interactions with light which can be quantified by their overlap integral as [20]

$$f = \frac{2\mu\omega}{\hbar} |\langle u_h | \, \mathbf{r} \cdot \hat{e} \, | u_e \rangle|^2 \frac{V}{\pi a_b^3} \tag{1.3}$$

where $\omega = E_X/\hbar$ is the frequency of the exciton resonance, $|u_{e,h}\rangle$ are Bloch wavefunctions of electron and hole respectively, and V is th quantization volume for the system under consideration. This quantity is called the oscillator strength of the excitons and is highly relevant to this thesis and the general field of exciton-polaritons.

1.1.2 Cavity Photons

A geometrical setup of reflectors, known as an optical cavity, is designed to confine light through multiple reflections, effectively trapping it within a defined space. If a photon enters the cavity at the resonance frequency it can have longer lifetimes inside the cavity compared to other frequencies. This spatio-temporal confinement leads to a significant increase in local photon density, enabling enhanced light-matter interactions, which are crucial for various applications in quantum optics.

Among the various optical cavity geometries, the simplest is the Fabry–Pérot [21] cavity (or planar cavity), which consists of two parallel mirrors facing each other (see Fig. 1.4a). As shown in Fig. 1.4b, the photonic modes in this system correspond to standing electromagnetic waves confined between the mirrors. The resonant wavelengths, λ_m, for this planar geometry and a mirror separation of L, satisfy $\frac{m \cdot \lambda_m}{2n_c} = L$ where $m = 1, 2, 3, \cdots$ and n_c being the effective refractive index of the cavity medium. The component of the wavevector, $\vec{\mathbf{k}}$, perpendicular the mirrors, $k_\perp$, is constant for a given mode order, m, and can be written as $k_\perp = n_c \frac{2\pi}{\lambda_m} = \frac{\pi m}{L}$. The energy for a cavity mode can then be expressed:

$$E_C = \frac{\hbar c}{n_c} |\vec{\mathbf{k}}| = \frac{\hbar c}{n_c} \sqrt{k_\perp^2 + k_\parallel^2} = E_0 \sqrt{1 + k_\parallel^2 / k_\perp^2} \quad \text{for} \quad E_0 = \frac{\hbar c k_\perp}{n_c} \tag{1.4}$$

where E_0 is the energy at normal inicidence ($k_\parallel = 0$). The disperison (or energy-momentum

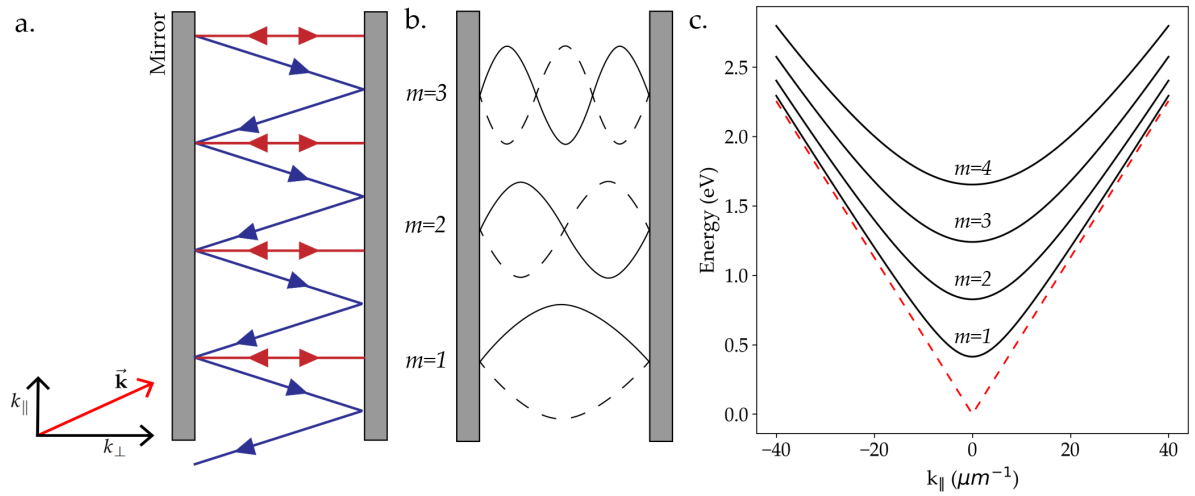

Figure 1.4: **Fabry–Pérot cavity. a.** The planar geometry of cavity. Red beam for $k_{\parallel} = 0$ and blue beam for $k_{\parallel} \neq 0$. **b.** First three cavity resonances for $k_{\parallel} = 0$, as standing waves between mirrors. **c.** Energy dispersion relation of the first four cavity modes with in-plane wavevector, for a typical cavity with $L = 1.5\ \mu m, n_c = 3.5$. The dashed line (red) shows the energy for an unconfined photon.

relation) for different cavity orders are presented in Fig. 1.4. For small angles when $k_{\parallel} << k_{\perp}$ we can approximate energies as,

$$E_C \approx E_0 + \frac{\hbar^2 k_{\parallel}^2}{2m_c} \quad \text{for} \quad m_c = \frac{E_0}{c^2/n_C^2} \tag{1.5}$$

This dispersion relation, at low momenta, resembles that of a massive particle (see Fig. 1.4c), allowing us to assign an effective mass to cavity photons propagating within the plane of the cavity for small in-plane wavevectors, $k_{\parallel}$. However, this effective mass is extremely small and of the order of $10^{-5} m_e$.

In this work, we primarily use the planar geometry, as shown in Fig. 1.4a. To achieve high reflectivity, we used dielectric mirrors known as distributed Bragg reflectors (DBRs). These mirrors consist of alternating layers of dielectric materials with contrasting refractive indices (see Fig. 1.5a). This periodic structure is designed to enhance constructive interference for reflected waves while suppressing transmission within a specific spectral range, known as the "stop band." Each layer is carefully engineered to be a quarter-wavelength thick at the designed central wavelength, λ_0, ensuring optimal reflectivity. A greater number of DBR layer pairs results in higher reflectivity and a flatter response within the stop band, as illustrated in Fig. 1.5b-e.

1.1.3 Strong coupling of excitons and photons

When an exciton hosting semiconductor layer is placed inside a microcavity and exhibits substantial spatial overlap with the cavity's electric field distribution, along with a spectral overlap of the resonances, the exciton-photon coupling is enhanced. The interaction between excitons and photons in this framework is commonly described using a simple two-level coupled os-

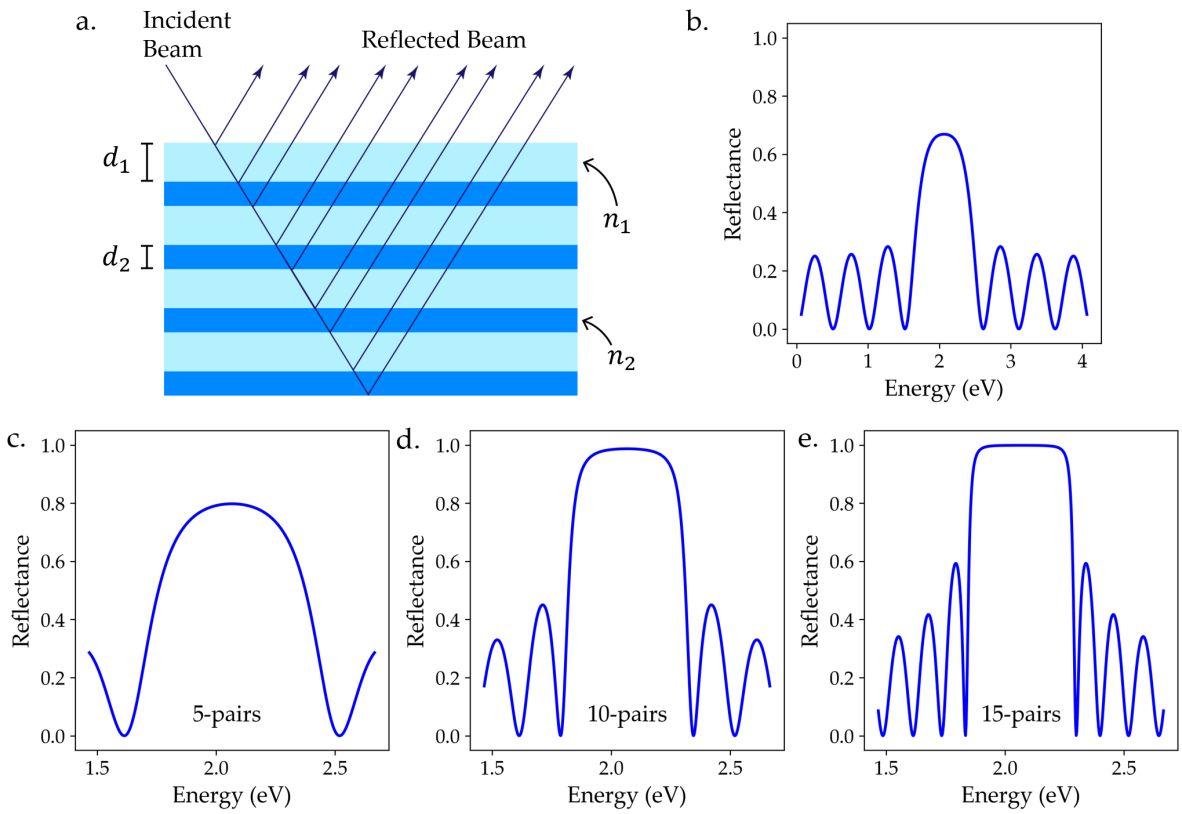

Figure 1.5: **A distributed Bragg reflector. a.** A schematic of a DBR with 4 pairs of alternating dielectrics. **b.** Reflectance for a DBR with parameters, $\lambda_0 = 600\ nm$, $n_1 = 1.5$, $n_2 = 2$ and having 4-pairs **c.** 5-pairs **d.** 10-pairs **e.** 15-pairs of alternating layers

cillator model. We can write the Hamiltonian as [20],

$$\widehat{H} = \begin{pmatrix} \widetilde{E}_x & V \\ V & \widetilde{E}_c \end{pmatrix} \tag{1.6}$$

where $\widetilde{E}_{x,c} = E_{x,c} + i\gamma_{x,c}$ are the complex oscillator energies where $E_{x,c}$ are the exciton and cavity photon peak energies with the decay rate $\frac{\gamma_{x,c}}{\hbar}$, respectively which are prportional to the linewidths. The coupling strength, V, depends on the exciton oscillator strength and the geometry of the cavity. The energy eigenstates for the Hamiltonian can be calculated as,

$$\widetilde{E}_{\pm} = \frac{(\widetilde{E}_x + \widetilde{E}_c)}{2} \pm \frac{1}{2}\sqrt{(\Delta - i\delta)^2 + 4V^2} \tag{1.7}$$

where $\Delta = E_c - E_x$ and $\delta = \gamma_c - \gamma_x$.

When $V < |\delta|/2$, the contribution by the second term in Eq. 1.7 is purely imaginary for $\Delta = 0$, hence eigenstates remain degenerate and no splitting is observed in terms of energy, as show in Fig. 1.6a and Fig. 1.6b.

When $V > |\delta|/2$, this exciton-photon mixture operates in the strong-coupling regime, where the energy eigenstates show anti-crossing behavior at $\Delta = 0$, as seen in Fig. 1.6c, and

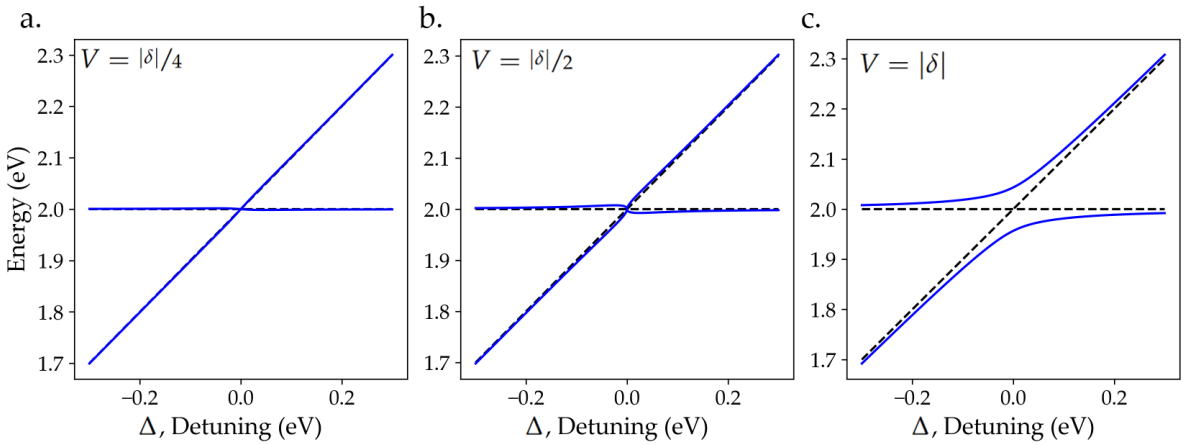

Figure 1.6: **Eigenenergies for a exciton-photon coupled system** as a function of their energy detuning, Δ, with the oscillator coupling strength, V **a** smaller, **b** equal to, and **c** larger than $|\delta|/2$, which is arbitrarily set to $\delta = 50\ meV$ to generate these plots.

the energy splitting between these branches is called Rabi splitting, Ω, and is given by,

$$\hbar\Omega = \mathfrak{Re}\left(\sqrt{4V^2 - i\delta^2}\right)$$

The split states are called the lower polariton (LP) and the upper polariton (UP) branches. We can simplify the calculations incorporating the Rabi splitting into a real valued eignenvalue equation for polaritons as,

$$\widehat{H}\begin{pmatrix} X \\ C \end{pmatrix} = \begin{pmatrix} E_x & \hbar\Omega \\ \hbar\Omega & E_c \end{pmatrix}\begin{pmatrix} X \\ C \end{pmatrix} = E_{\pm}\begin{pmatrix} X \\ C \end{pmatrix} \tag{1.8}$$

where $\begin{pmatrix} X \\ C \end{pmatrix}$ is eigenvector satisfying the normality condition $|X|^2 + |C|^2 = 1$. Here, $|X|^2$ and $|C|^2$ are the Hopfield coefficients and are defined as the exitonic and photonic fractions, respectively. These fractions depends on the Rabi splitting of the system and detuning between resonances and are given by,

$$|X, C|^2 = \frac{1}{2}\left(1 \pm \frac{\Delta}{\sqrt{\Delta^2 + (2\hbar\Omega)^2}}\right)$$

Using the expression for energies of cavity mode and the exciton for small in-plane momenta, we can write the polariton Hamiltonian as,

$$\widehat{H} = \begin{pmatrix} E_x + \frac{\hbar^2 k_{\parallel}^2}{2(m_e + m_h)} & \hbar\Omega \\ \hbar\Omega & E_0 + \frac{\hbar^2 k_{\parallel}^2}{2m_c} \end{pmatrix}$$

and since it is known that $m_c << m_e$, we can consider the exciton dispersion to be flat for small in-plane momenta. We use this approximation to generate energy-momentum relation (dispersion) of UP and LP branches, shown in Fig. 1.7a-c. Note that three different exciton-

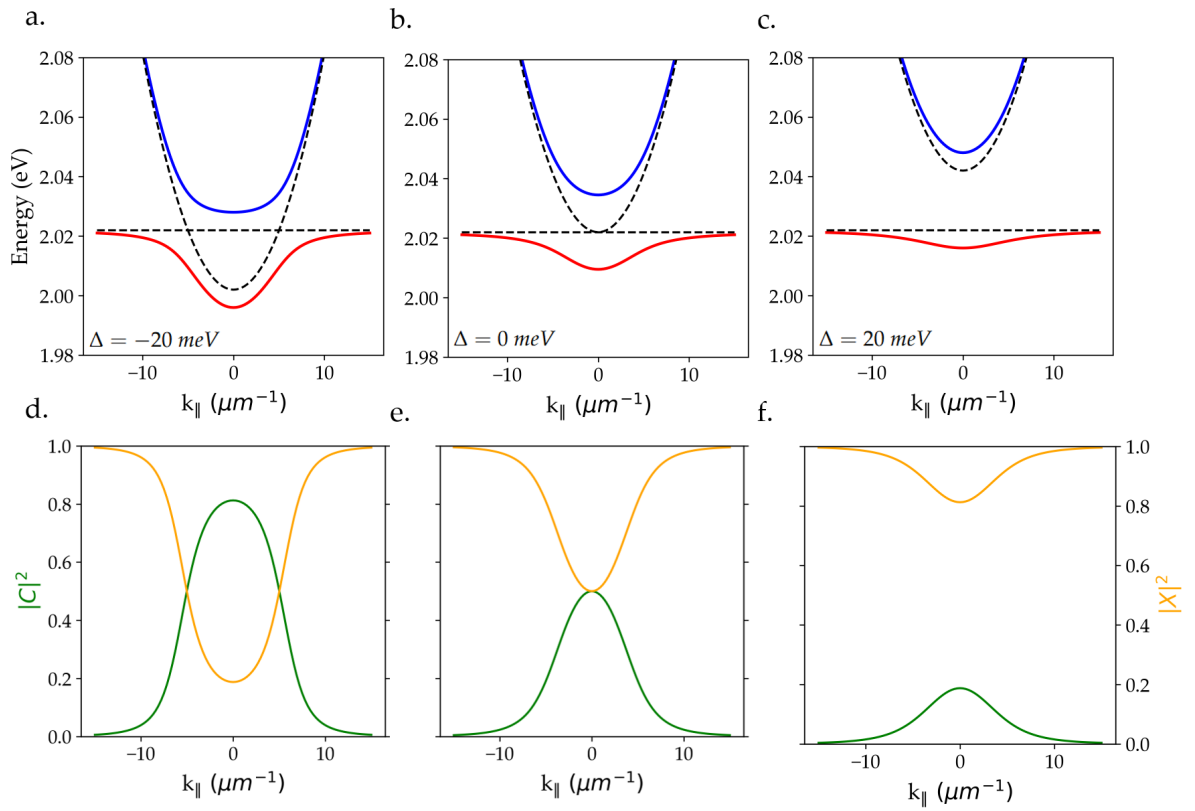

Figure 1.7: **Analytically derived properties of polaritons in an optical microcavity at different detunings as function of in-plane wavevector. a-c** Eigenenergies for upper polariton (blue) and lower polariton(red) for $2\hbar\Omega = 50\ meV$. Dashed line depicts uncoupled energies. **d-f** Corresponding Hopfield coefficients for the lower polariton branch from panels a-c

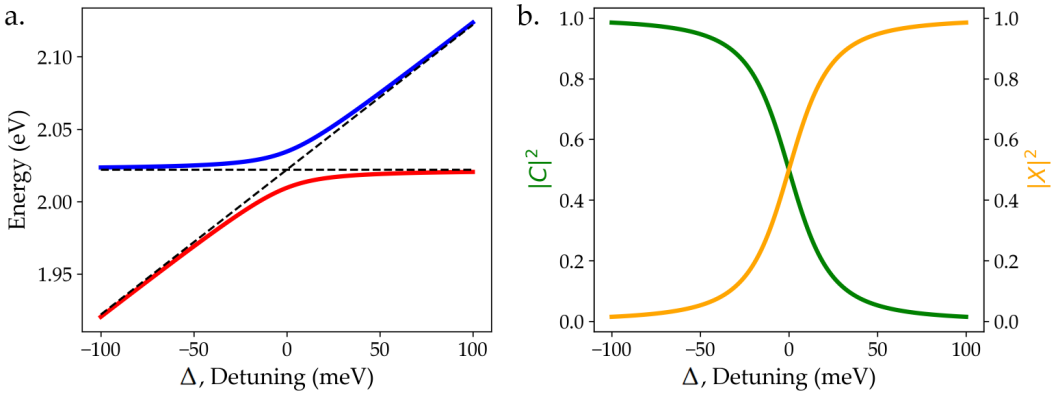

Figure 1.8: **Analytically derived properties of polaritons, at normal incidence, as function of detuning. a.** Eigenenergies of the UP (blue) and LP (red) at $k_{||} = 0$. **b.** Hopfield coefficients for the LP branch at $k_{||} = 0$.

photon detunings at $k_{||} = 0$ are shown. Furthermore, the $k_{||}$-dependence on the excitonic and photonic fractions of LP branch, as calculated for the same detunings, are presented in Fig. 1.7d-f. Note that for high $k_{||}$, LP becomes purely excitonic which is expected as the photon dispersion diverges away from the excitonic one. The behavior at $k_{||} = 0$ as a fuction of exciton-photon detuning is shown in Fig. 1.8, as the detuning gets more positive (negative) the LP

becomes more excitonic (photonic). Fig. 1.8a is what we usually get in experiments and the identification of the Rabi splitting is crucial in determining the existence of strong-coupling.

1.2 Transition Metal Dichalcogenides

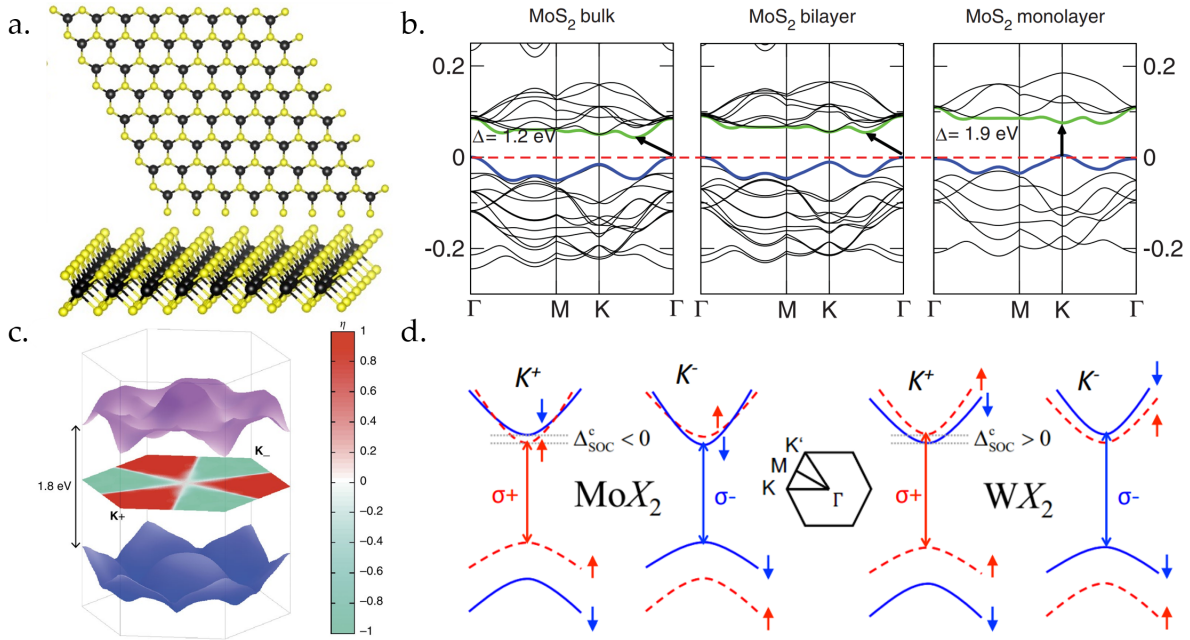

Figure 1.9: **Transition Metal Dichalcogenides a.** Ball and stick representation of TMDs (MX_2), Black represents metal (M) atom while yellow represents dichalocgenide (X) atom. **b.** Electronic band structure for bulk, bilayer and monolayer MoS_2, indirect band gap in bulk to direct band gap in monolayer, adapted from [4]. **c.** Band structure in 2D $k-$space. Valleys lie at the hexagonal Brillouin zone's vertex. The color plot shows the degree of circular polarization for the interband transition. Adapted from [5]. **d.** Fine splitting of the valleys due to spin-orbit coupling depending on the metal atom. Adapted from [6].

Excitons can be hosted by different semiconductor materials. Early works on exciton polaritons are based on III-V semiconductors, such as GaAs and CdTe, but the small exciton binding energies in these systems only allow cryogenic operation. In this work, I focus on 2D materials, specifically transition metal dichalcogenides, where interlayer excitons can readily form and are stable at room temperature.

Transition metal dichalcogenides (TMDs) are a class of van der Waals (vdW) materials with the general formula MX_2, where M is a transition metal (e.g., Mo, W) and X is a chalcogen (e.g., S, Se, Te). Each monolayer consists of a hexagonal arrangement of metal atoms sandwiched between two chalcogen layers in an X–M–X configuration (see Fig. 1.9a). These layers are held together by weak vdW forces [22], allowing easy mechanical exfoliation.

Bulk TMDs typically exhibit an indirect band gap due to interlayer interactions that modify their electronic structure. However, in the monolayer limit, they transition to a direct band gap at the K-points in the hexagonal Brillouin zone [23]. These points, known as K-valleys (see Fig. 1.9b-d), are related only by time-reversal symmetry and therefore possess opposite angular momenta. As a result, when electrons and holes are excited, they predominantly form

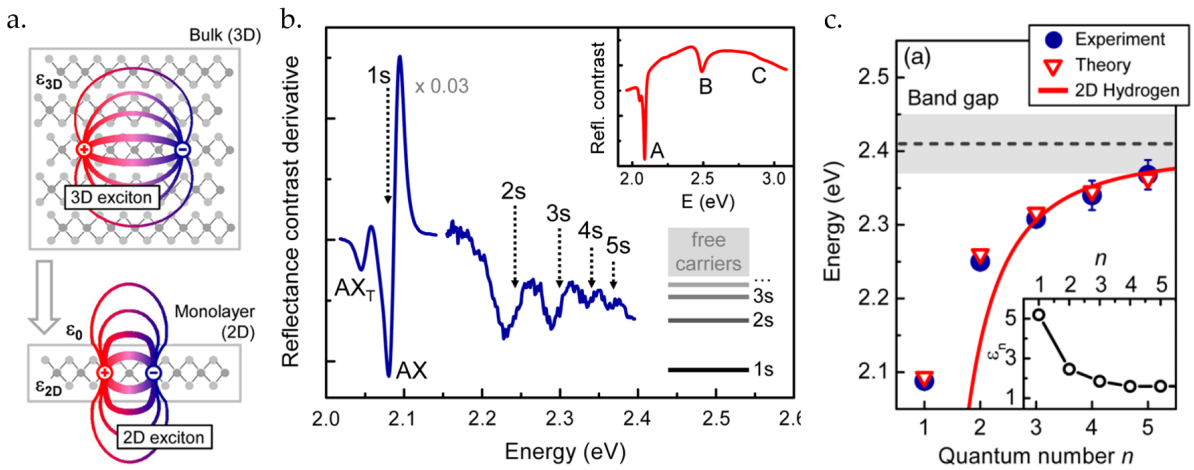

Figure 1.10: **2D exciton in TMDs. a.** A schematic diagram showing the reduced screening of Coulomb interaction upon dimensional restriction. **b.** Derivative of reflectance contrast plot, depicting transitions higher excitonic states. **c.** The deviation of energies from the 2D hydrogen model.

excitons within these valleys. These excitons dominate the optical response of TMD monolayers, making them ideal platforms for studying exciton physics, light-matter interactions, and potential applications in optoelectronics and quantum technologies [6].

1.2.1 Excitonic Properties

Using the 2D hydrogen model approximatio, the exciton states in 2D materials have binding energies of

$$E_X(n) = Eg - \frac{\mu e^4}{2\hbar^2 \epsilon^2 (n - 1/2)^2}$$

However, experiments probing this energy series show a strongly deviating behavior [24] due to increased screening as size increases (see Fig. 1.10). The reduced dielectric screening in monolayer TMDCs results in tightly bound excitons with Bohr radii ranging from approximately 1 to 1.5 nm [7] and binding energies on the order of a few hundred meV [24, 25, 7]. These binding energies are significantly higher compared to conventional bulk semiconductors like GaAs.

The strong binding energy and spatial confinement of excitons in TMDC monolayers have several important implications. Firstly, the high binding energy ensures exceptional stability, allowing excitonic resonances to remain well-defined and easily observable even at room temperature where thermal energy is $k_b T \approx 26\ meV$. Additionally, the close proximity of electrons and holes within the monolayer results in significant wavefunction overlap, leading to a strong interaction with light. The oscillator strength for this interaction, confined in one-dimension, is given by [26, 20]

$$f = \frac{2}{\mu\hbar\omega} |\langle u_h | \hat{e} \cdot \mathbf{p} | u_e \rangle|^2 |\langle F_h | F_e \rangle|^2 \frac{V}{\pi a_b^3}$$

where u_e and u_h are the lattice periodic (Bloch) parts of the electron and hole wave functions, F_e and F_h are the envelope wave functions of electron and hole, $\hat{e}$ is the polarization vector, $\mathbf{p}$ is the

momentum operator and V is the quantization volume of the exciton. The term $|\langle F_h|F_e\rangle|^2$ accounts for the quantum confinement in the reduced dimension and $\frac{V}{a_{B,2D}^3}$ describes the enhancement of the electron and hole wave function overlap due to the exciton formation. However, since TMDC monolayers are so strongly confined and are therefore close-to-ideal 2D systems, the latter contribution is considered to have a $\frac{1}{a_{B,2D}^2}$ dependence [24]. The large wave function overlap also results in a very fast radiative decay time τ_0. The radiative decay time is defined by the radiative decay rate (Γ_0 as $\tau_0 = \frac{1}{\Gamma_0}$), which in turn is described by Fermi's Golden rule,

$$\Gamma_0 \sim |\langle f'|\hat{e}\cdot\mathbf{p}|i\rangle|^2 \rho_r(\Delta E)\,\delta(\Delta E - \hbar\omega)$$

where i and f' are the initial and final states, $\rho_r(\Delta E)$ is the combined density of states and $\delta(\Delta E - \hbar\omega)$ is a delta function, which describes energy conservation. In fact, radiative lifetimes of a few hundred fs to one ps have been measured for TMDC monolayers[27, 28], which has been confirmed by first principle calculations [27, 29].

Furthermore, due to the atomic-scale thickness of monolayers, their excitonic properties are highly sensitive to the surrounding dielectric environment, including the substrate or any capping material [25, 30]. In this Thesis, I explored two 2D materials. The first is monolayer WS_2, which exhibits exceptional optical properties at room temperature, including bright photoluminescence and large oscillator strength. The second is homobilayer 2H-MoS_2, which hosts interlayer excitons with permanent out-of-plane dipole moments, allowing for electrical tunability and nonlinear excitonic interactions. These properties make 2H-MoS_2 a promising candidate for studying polariton-based superconductivity.

1.2.2 Charge Doping and Polarons

Imbalances in electron and hole densities within TMD monolayers, along with the corresponding detuning of their Fermi energy, can significantly alter their optical response [31, 32] Specifically, an increased electron (hole) density in the conduction (valence) band leads to the formation of charged excitons, also known as trions, where a neutral exciton binds to an additional electron or hole [33]. These quasiparticles exhibit distinct optical signatures compared to neutral excitons, including reduced transition energies and modified linewidths due to many-body interactions [34]. One effective way to control exciton and trion populations is by electrostatic gating, which allows precise tuning of the Fermi energy via an applied gate voltage, as in [31, 32]. The transition energy of trions is lower than that of neutral excitons, with the energy difference corresponding to the binding energy of the extra charge, typically around 30 meV for WS_2 [35, 33]. Furthermore, at sufficiently high doping levels, excitonic features weaken as free carriers screen Coulomb interactions, leading to a crossover from excitonic to many-body Fermi polaron states [36]. These states consists of an exciton being embedded in a Fermi sea of free charge carriers.

In this Thesis, I have explored charge doping as a means to manipulate excitonic properties in 2D materials and I discuss how controlled charge doping influences the excitonic properties in bilayer MoS_2.

1.2.3 Effects of External Fields

The excitonic properties of TMDs can be significantly modified by applying external electric and magnetic fields. As mentioned earlier, excitons in monolayer TMDs are formed within the K-valleys, which are energetically degenerate but possess opposite spins and, consequently, opposite magnetic dipole moments. The application of a strong out-of-plane magnetic field lifts this valley degeneracy through the Zeeman effect (see Fig. 1.11c), resulting in energy splitting between the excitons in opposite valleys [7].

While monolayer excitons have small, randomly oriented dipole moments and are largely unaffected by electrostatic fields, bilayer TMDs host interlayer excitons, where the electron and hole reside in different layers. These excitons possess a permanent out-of-plane dipole moment, making them highly sensitive to external electric fields. By applying a perpendicular electric field, the energy of interlayer excitons can be continuously tuned due to the linear Stark effect [8]. A simultaneous application of voltage gating and an in-plane electric field has been shown to effectively create confined neutral excitonic states through the quadratic Stark effect and density-dependent interactions [9]. Furthermore, this technique has been employed to engineer the exciton wavefunction, providing enhanced control over excitonic properties in TMD monolayers [20]. These advancements pave the way for precise manipulation of excitonic states, offering new opportunities for tunable exciton-based optoelectronic and quantum devices utilizing 2D materials.

Previous works have focused on magnetic fields and out-of-plane electric fields. In this Thesis, I explored the effectof an in-plane electric field, particularly on interlayer excitons in bilayer MoS_2. This provides an additional degree-of-control over the optical properties.

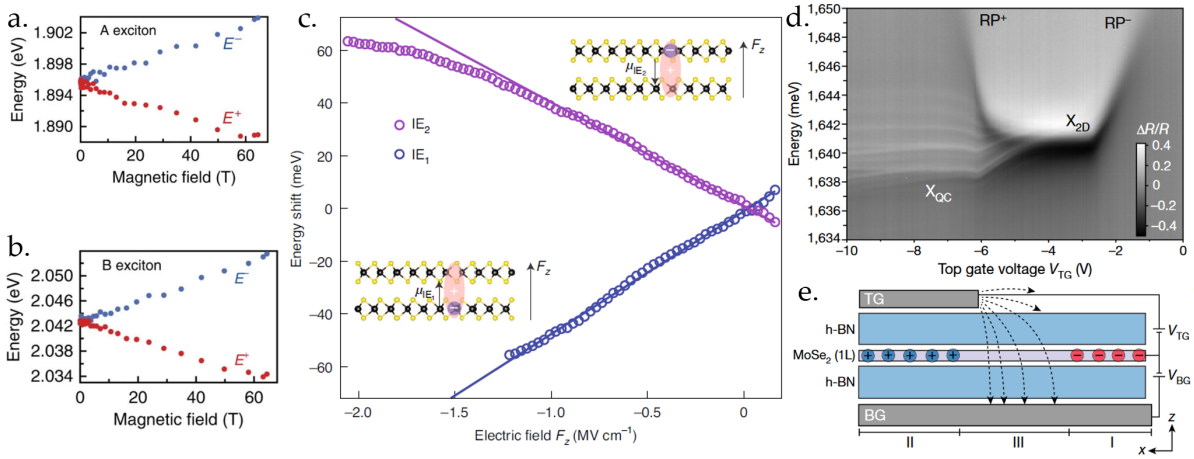

Figure 1.11: **Tunability of excitonic properties. a-b.** Zeeman splitting for A and B exciton in monolayer MoS_2, adapted from [7]. **c.** Linear Stark effect for IL exciton in bilayer MoS_2, adapted from [8]. **d.** Quantum confinement and formation of discrete excitonic using the density interactions and an in-plane electric field. **e.** Schematic of the configuration used in **d**, adapted from [9].

1.3 Sample Preparation Techniques

This section outlines the fabrication techniques employed to prepare the samples used in this work. These include micromechanical cleavage of TMD flakes and their deterministic transfer for precise positioning. Additionally, we describe the photolithography process used for electrode patterning on the substrate, which is used to apply in-plane electric fields.

1.3.1 Micromechanical Cleavage

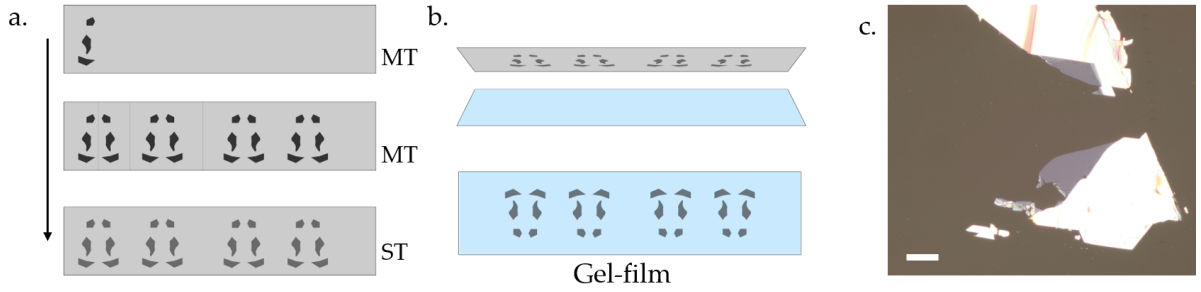

Figure 1.12: **Process of exfoliation. a.** Peeling off layers using a tape and thinning down the flakes. **b.** Transferring the contents onto a Gel-film. **c.** An optical microscope image of 2 bilayers along with bulk flakes on a Gel-film. Scale bar is of 20 μm.

Since the individual layers of TMD crystals are held together by weak van der Waals interactions, these can be separated into monolayers using micromechanical cleavage (exfoliation) as first shown by *Novoselov et al.* [37] for graphene and later for TMDs [23]. To prepare the monolayers and bilayers used in this work, we used a commercially available Scotch Tape. We carefully slice thin crystals (flakes) from bulk crystals sourced from HQ Graphene and place them onto one end of the tape (see Fig. 1.12a). By repeatedly folding and unfolding the tape, we created multiple thinner flakes, forming what we refer to as the master tape (MT). A fresh piece of tape was then used to peel off thinner flakes from the MT, creating a secondary tape (ST).

This process was repeated several times to progressively thin down the flakes. Once sufficiently thinned, one of the STs was selected and transferred onto a Gel-Pak polydimethylsiloxane (PDMS) gel film. Moderate pressure was applied to facilitate optimal transfer, as adhesive forces are weaker on the gel film compared to the tape. The tape was then swiftly removed, leaving behind flakes on the Gel-film (Fig. 1.12b), which was subsequently inspected to identify monolayers. We use an optical microscope to search for monolayers and bilayers as the optical contrast on the Gel-film characterizes the thickness of the flakes as shown in Fig. 1.12c.

1.3.2 Deterministic Dry Transfer

Once we identify the desired flakes, we transfer them onto dedicated substrates (DBR or Si/SiO2)for further use. This process is carried out using a custom-built transfer setup, which allows for precise alignment of the substrate and flakes on the Gel-film with micrometer accuracy. The transfer setup comprises a sample holder mounted on a XY translation stage and a

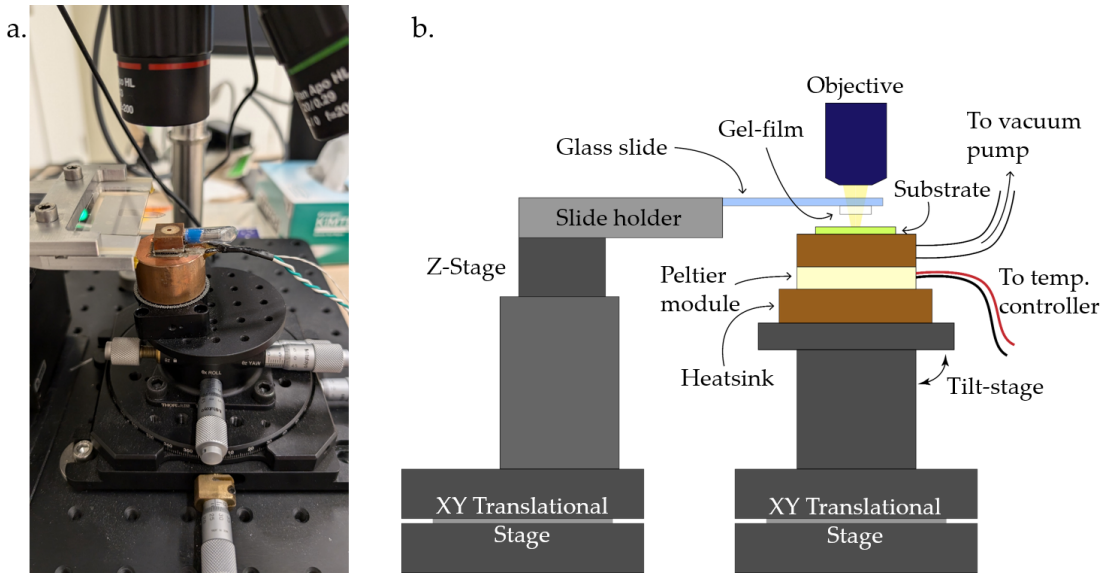

Figure 1.13: **Transfer Stage a.** A picture **b.** A schematic diagram of the custom transfer setup used in this work.

microscope glass slide holder for placing the Gel-film, which is attached to a XYZ translation stage. The sample holder integrates a custom-built heating and cooling system based on a Peltier module, regulated by a bipolar temperature controller for precise temperature adjustments. Additionally, a vacuum pump secures the sample in place during transfer. An optical microscope, capable of focusing on both the sample holder and the microscopic slide mount, enables real-time monitoring, ensuring precise alignment between the monolayer and the target substrate before bringing them into contact.

We cut out the desired portion of the gel film and place it onto the glass slide. For high-precision transfers, we carefully trim the gel film to the smallest possible size while ensuring that the target flake remains undamaged. Once the desired position is identified, the substrate is heated to 60°C to facilitate the transfer. Using the Z-actuator, the flake is gradually lowered until it makes contact with the substrate. Upon contact, the air gap between the Gel-film and the substrate begins to close in a controlled manner from one direction. As the Gel-film is gradually lowered, the gap continues to shrink until the entire monolayer area makes full contact with the substrate surface. The Gel-film is lifted at a moderate speed, ensuring a clean and successful transfer of the monolayer while minimizing strain or damage to the flake.

1.3.3 Photolithography

For gold electrode patterning (used to induce electric field), we used photolithography, a widely used microfabrication technique in which a photosensitive material (photoresist) is coated onto the substrate and selectively exposed to UV light to define patterns for metal deposition, such as chromium and gold.

As shown schematically in Fig. 1.14. We first coat the substrate with a positive photoresist, AZ 1514 H, using a spin coater at 4000 rpm for 40 seconds to achieve a thin, even layer. The coated substrate is then soft-baked on a hot plate at 80°C for 120 seconds to remove excess

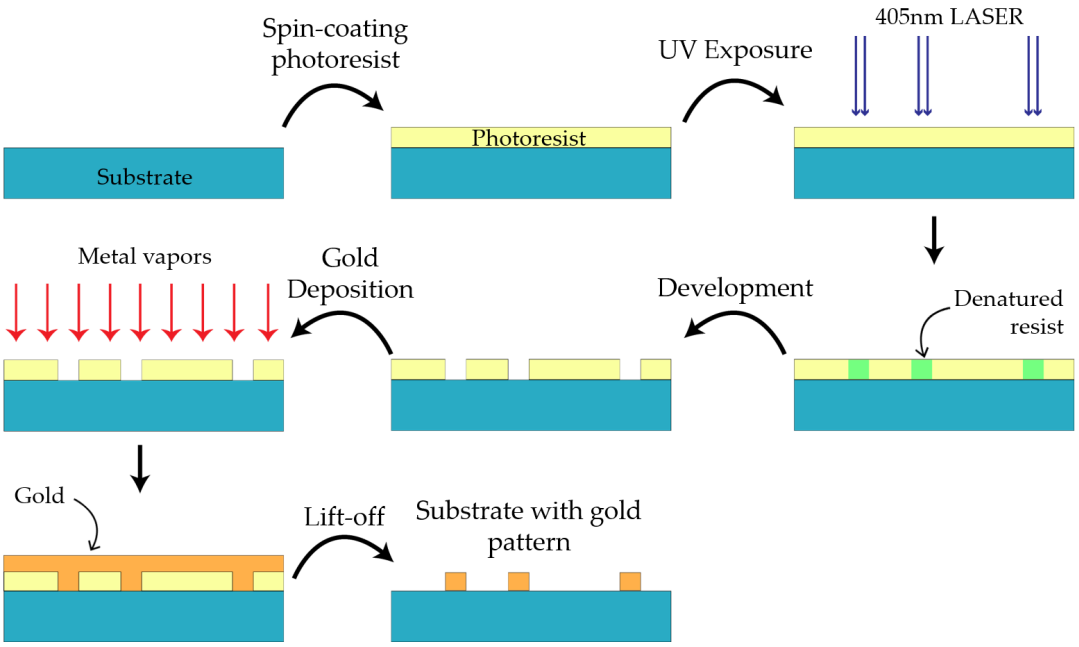

Figure 1.14: **Photolithography.** A schematic diagram showing the process of pattering gold electrodes on a substrate.

solvents and improve adhesion.

Next, we expose the coated substrate to a 405 nm laser using the Heidelberg Instruments MLA 150 Maskless Aligner. This direct-write lithography system allows for precise patterning without the need for physical masks. Since we use a positive photoresist, the exposed regions lose their polymeric structure and become soluble in a dedicated developer. The development process is carried out using AZ 726 MIF developer, where the exposed regions are dissolved, leaving behind the desired pattern.

Following successful patterning, we deposit metal contacts using the Temescal BJD-2000 Electron-Beam Evaporator. A thin adhesion layer of 10 nm chromium is first deposited to promote strong bonding between the gold and the substrate, followed by a 60 nm gold layer to form the electrodes. These metals are deposited under high vacuum to ensure high purity and uniformity.

Finally, we perform a lift-off process using acetone. The substrate is immersed in acetone and subjected to gentle agitation, dissolving the remaining photoresist and lifting off the excess metal, leaving behind well-defined gold electrodes on the substrate. The sample is then rinsed with isopropanol and dried with nitrogen to remove any residual contaminants.

All the processes mentioned above were carried out at Australian National Fabrication Facility's ACT Node.

1.4 Spatially- & Angle-resolved Spectroscopy

The optical characterization of the samples prepared in this work relies primarily on the measurement of photoluminescence (PL) and reflectivity spectra. The experimental setup we used, as shown in Figure 1.15, is designed to enable both real-space (RS) and momentum-space (KS)

imaging with a sub-micron spatial resolution. The setup can be divide into three separate sections - excitation arm, sample handling and detection arm.

Excitation Arm

The excitation arm consists of a Nd:YAG frequency doubled continuous wave (CW) laser source with emission wavelength of $\lambda = 532\ nm$ $(E \approx 2.33\ eV)$. An acousto-optic modulator (AOM) is placed after the laser to generate quasi-cw pulses (larger than tens of nanoseconds) with a tunable pulse duration and repetition rate. It also consists of halogen broadband light source (ThorLabs SLS201L/M) for reflectance measurement and normal imaging. Using the flip mount mirror (FM1), we are able to switch between these sources for PL and reflectivity measurements, respectively. The excitation beam is directed towards a beam splitter cube (BSC1), which redirects it to the sample. Additionally, a flip lens (FL3) can be introduced into the beam path, expanding the illumination spot on the sample, hereafter referred to as the "big spot" configuration.

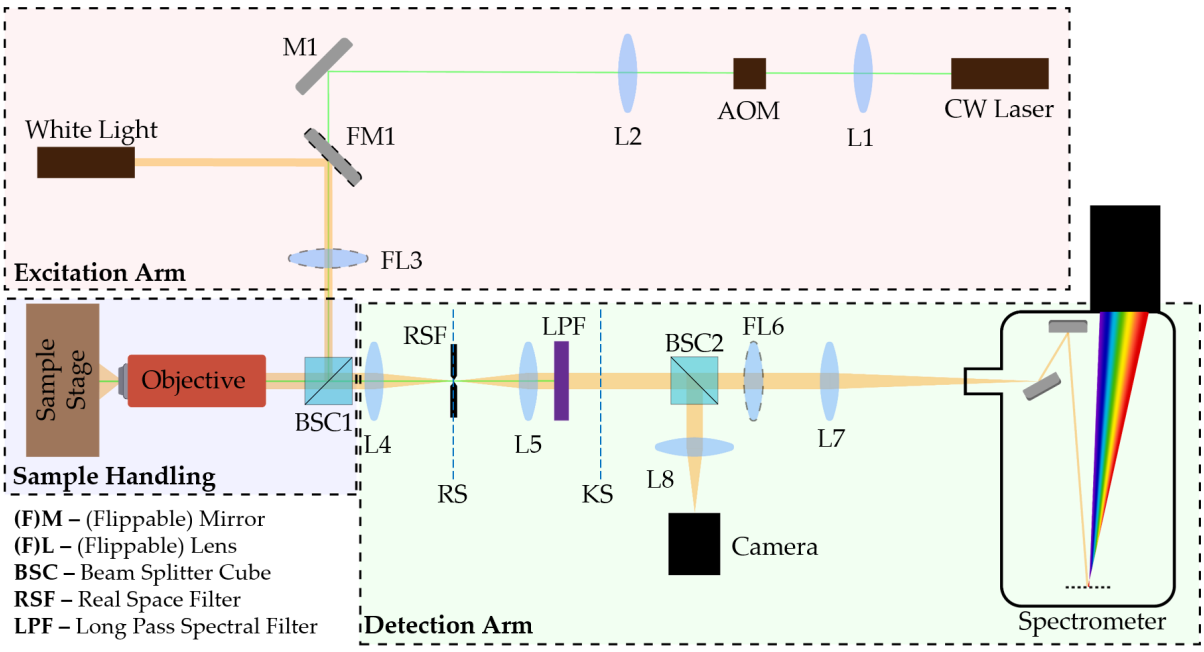

Figure 1.15: **Layout of the optical characterization setup.** The setup is used for angle- and spatially-resolved PL and reflectivity spectroscopy. It allows for preliminary imaging, spatial filtering and multiple access points to both KS and RS, if needed.

Sample Handling

This section consists of a 50X Mitutoyo Plan Apo NIR HR Infinity-Corrected Objective (NA = 0.65, FL = 4 mm, WD = 10 mm), which focuses the excitation beam from BSC1 onto the sample and collects the re-emitted or reflected light over a broad range of angles. The maximum angle,

θ_{max}, that can be collected is given by:

$$\theta_{max} = \arcsin\left(\frac{\text{NA}}{n_{\text{medium}}}\right)$$

which for this objective and $n_{\text{medium}} = 1$ is $\theta_{max} \approx 40.5°$. This angle corresponds to an in-plane wave-vector of $k_{\parallel} \approx 6.8\ \mu m^{-1}$ for a wavelength of 600 nm. The collected light is then transmitted towards the detection arm through BSC1. The samples are mounted on a XYZ micrometer translation stage, allowing for precise positioning and focusing relative to the objective.

Detection Arm

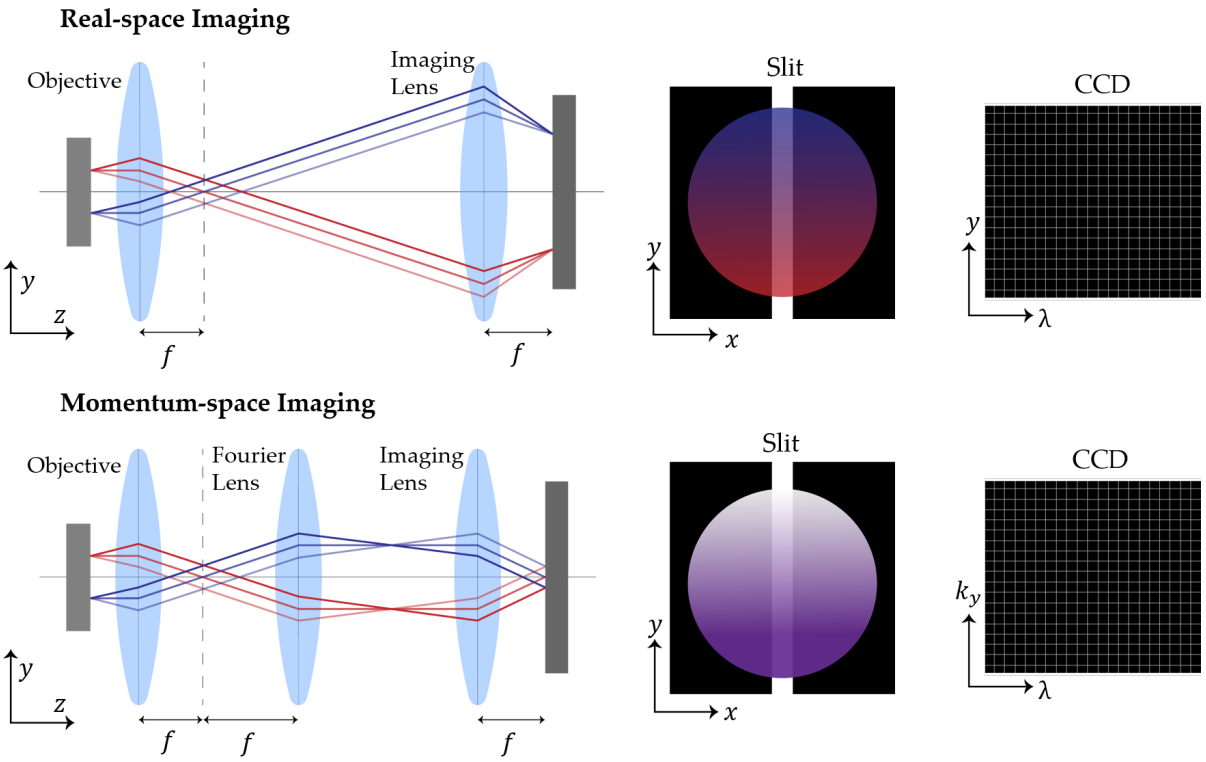

Figure 1.16: **Real and Momentum space imaging.** The spatial position of a ray is encoded in the color while the angle is encoded by the opacity of the ray. To image RS, we only need to focus the light collected by objective on to the detector using a lens. The slit then selects a thin slice of 'y'. To image KS, we use an additional lens that acts as an objective for the back focal plane of the main objective. This allows for imaging the Fourier transform of the sample and hence is called a Fourier lens. The slit then selects a thin slice of 'k_y'.

This arm consists of a series of lenses that are arranged in order to provide access to both real-space (RS) and momentum-space (KS). It leverages property of lenses to perform Fourier transformations in their focal planes (see Figure 1.16). The objective creates a KS image on its back focal plane, which is then transformed back to a RS image by L4 ($f = 150\ mm$). We use an adjustable XY slit (RSF) to filter in the desirable region on the sample. The filtered signal is converted back to KS by L5 ($f = 150\ mm$). A long-pass filter is used here to suppress the laser excitation beam reflected off the sample while transmitting the PL signal. Using BSC2

and L8, an RS image is formed on a camera for preliminary imaging. The unreflected beam is focused onto the spectrometer slit using L7 ($f = 250\ mm$). The imaging mode is determined by the state of the FL6 lens—when FL6 is in the beam path, the system captures angle-resolved spectra, while removing it allows sparially-resolved spectroscopy.
We use the *Andor Shamrock 500i* spectrograph to measure the spectra. It is equipped with *Andor iXon 888 EMCCD* camera and a set of interchangeable spectrometer gratings with 150 l/mm, 600 l/mm, and 1200 l/mm which allows for a spectral resolution of 0.58 meV, 0.14 meV, and 0.06 meV, respectively. The choice of grating enables flexibility in balancing spectral resolution and signal intensity, depending on the specific experimental requirements. Additionally, the CCD has a pixel dimensions of $13 \times 13\ \mu m^2$. Combined with the objective and the array of relay lenses used, this configuration results in a spatial resolution of about $0.2\ \mu m$/pixel.

Chapter 2

Open Micro-Cavity: Design and Characterization

Integrating two-dimensional materials inside a microcavity typically requires depositing a dielectric directly on top of the 2D material. Unfortunately, the deposition can degrade the optical properties of these materials [38]. In this Chapter, I focus on designing a structure that circumvent this direct deposition. We use an open cavity design where there is an air gap between the monolayer and the top mirror, such that the 2D material retains its optical properties.
In order to investigate strong light-matter coupling within TMDs, we designed a tunable open microcavity—'open' indicating the absence of a spacer medium and 'tunable' referring to its variable cavity length. The former enables easy access to the sample, e.g. for electrical contacting, and the latter ensures variability of the energy detuning between the cavity photon and exciton, which results in polaritons with a varying photonic/excitonic content (see Section 1.1). The aspects of the design that we focused on were its:

1. **Compactness**, as the ultimate goal is to integrate the cavity into a cryostat, where space constraints are significant.

2. **Reusability and robustness**, as per the cavity needs to accommodate different mirrors and materials while remaining structurally stable once assembled.

2.1 The Design

The cavity design, as shown in Fig. 2.1, consists of two DBRs, grown on fused silica substrates which are transparent to visible wavelengths, positioned to face each other and clamped between two precisely machined metal plates. We used two sets of DBRs composed of alternating layers of SiO_2 and Ta_2O_5, one with 10 pairs and another with 16 pairs. The DBRs were grown by ion beam sputtering (IBS) at the Australian National Fabrication Facility's (ANFF) OptoFab node. The optimal configuration for our experiments is the one with the 10-pair DBR as the top mirror and the 16-pair DBR as the bottom mirror, as the transmission at 532 nm for 10-pair DBR is double ($\sim 8\%$) the value for 16-pair DBR ($\sim 4\%$). This arrangement facilitates better

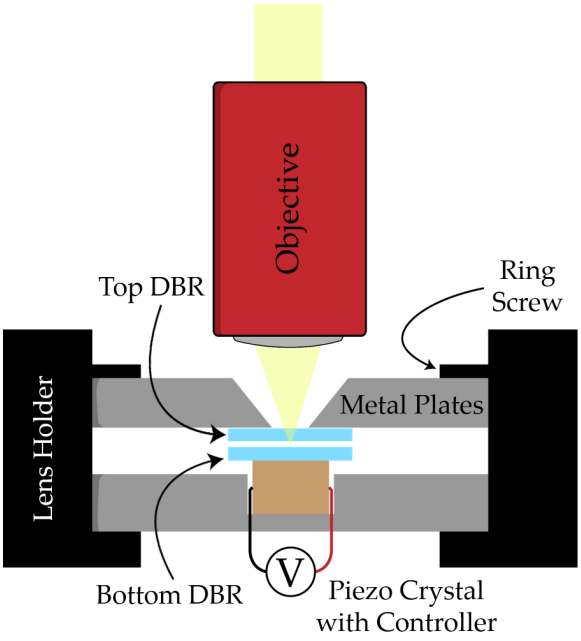

Figure 2.1: Schematic of the designed open microcavity.

excitation using the CW laser while the 16-pair DBR at the bottom provides higher reflectivity and in turn a higher finesse enabling most of the PL to be directed back towards the detection path.

The bottom DBR is mounted on a piezoelectric actuator crystal (ThorLabs PA4FKW), which enables fine control over the cavity spacing. As shown in Fig. 2.2a, the actuator is rigidly affixed to the bottom plate and under free load it is expected to provide a displacement of 3.6 μm at a 150V. The top plate has a tapered hole to allow optical access to the mirrors and collection of light at large angles, enabling the access to higher in-plane momentum, which is crucial for detecting the full dispersion of the cavity. To apply a voltage bias across the piezo actuator we use the ThorLabs K-Cube Piezo Controller (KPC101) which is designed to work in a 0-150V range and low current. The entire assembly is screwed with a retaining ring

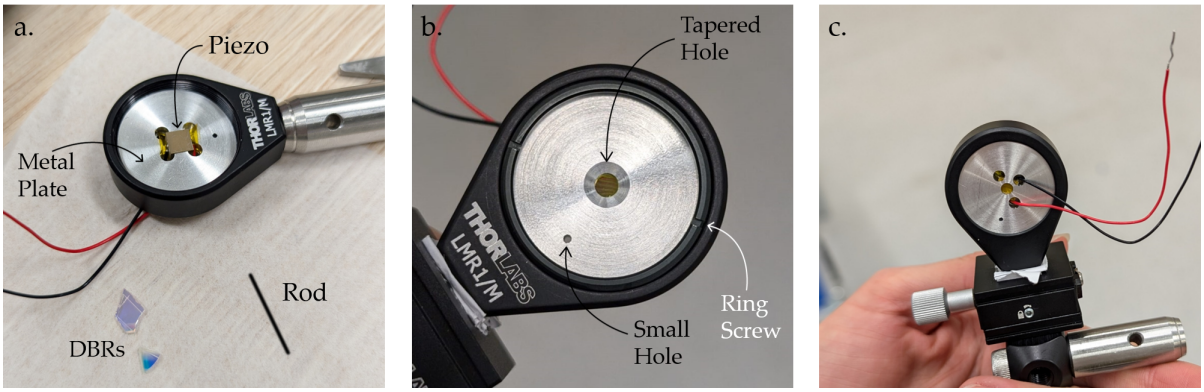

Figure 2.2: **The cavity a.** from inside **b.** from top **c.** from bottom

screw inside a 1-inch lens holder. This provides additional mechanical stability and prevents any relative displacement between components. A metal rod is inserted through small holes

in both plates during assembly to prevent them from rotating when the screw is tightened. Once there are few fringes visible by naked eye on the cavity through the tapered hole which are fairly spaced, we proceed with the optical characterization of the cavity using the setup described in Section 1.5.

2.2 Characterization

To validate and characterize our design, we initially assembled an empty cavity without piezoelectric control. The angle-resolved white light reflectance spectrum was measured for this configuration. In the spectrum (see Fig. 2.3), two distinct peaks in the DBR's stop band region are clearly visible at 2.03 eV $(610\ nm)$ and 2.23 eV $(556\ nm)$ at normal incidence. These modes correspond to two consecutive longitudinal resonances of the cavity.

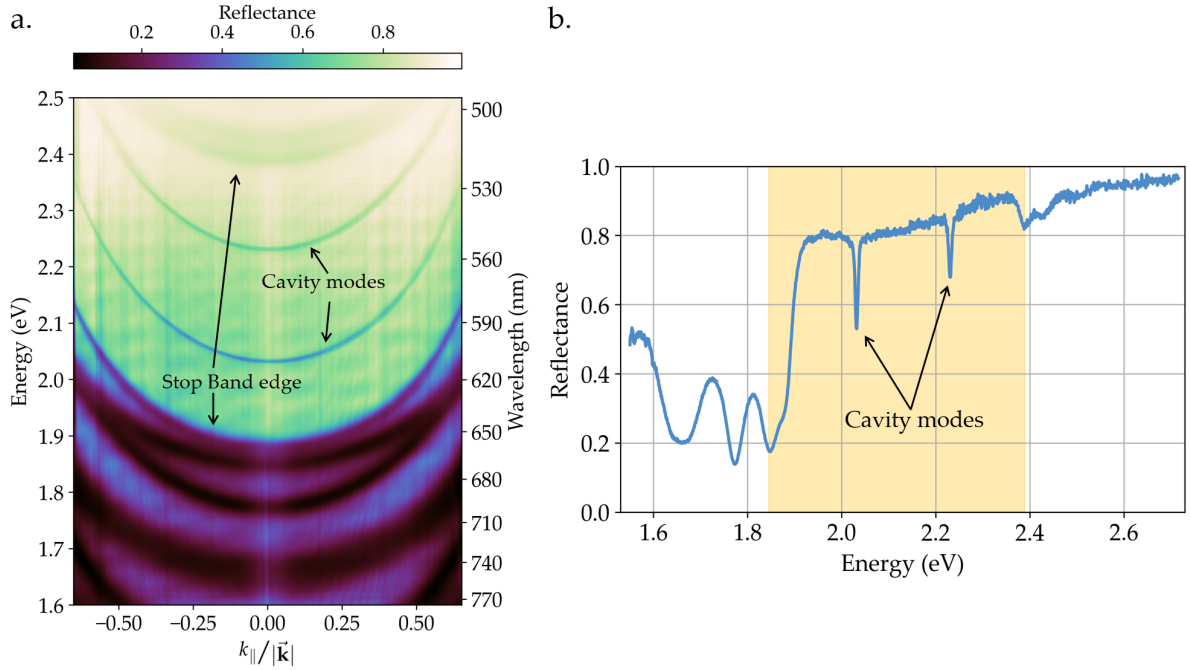

Figure 2.3: **a.** Angle-resolved reflectance spectrum of the open-cavity **b.** Cross-section at normal incidence ($k_{\|} = 0$), cavity modes at 2.03 eV and 2.23 eV. The shaded region marks the stop band region for the DBRs used. The values above around 550 nm become unreliable due to B anti-reflection coating on optics used but band edge still be qualitatively identified especially in angle-resolved spectrum .

We can calculate the cavity spacing using the relation,

$$L = \frac{\lambda_m \cdot \lambda_{m+1}}{2(\lambda_m + \lambda_{m+1})}$$

where λ_m and λ_{m+1} are wavelengths for two consecutive modes. This comes out to be approximately 3.1 μm, which is small enough to facilitate significant strong coupling. Note that this is the effective cavity length and not the air gap. The DBR being an extended structure has a finite penetration depth, L_τ, defined as the distance at which a fixed-phase mirror has to be

displaced in order to produce the same phase delay upon reflection [39]. It is given by,

$$L_\tau = \frac{\tanh(kl)}{2k} \quad \text{for} \quad k = \frac{2\Delta n}{\lambda_0}$$

where λ_0 is the central wavelength of DBR, Δn is the difference between the refractive indexes of SiO_2 and Ta_2O_5 at λ_0, and l is the total thickness of the DBR. This along with a quarter wavelength for the top layer adds approximately 0.32 μm to the air gap at each DBR. This makes the estimated air gap for this cavity to be 2.5 μm. Additionally, we determine the order of these modes using the relation, $m = {}^{2L}/_{\lambda_m}$. For the lower energy mode this order is $m = 10$. In principle, a lower mode order allows for a broader tuning range for the same change in cavity length.

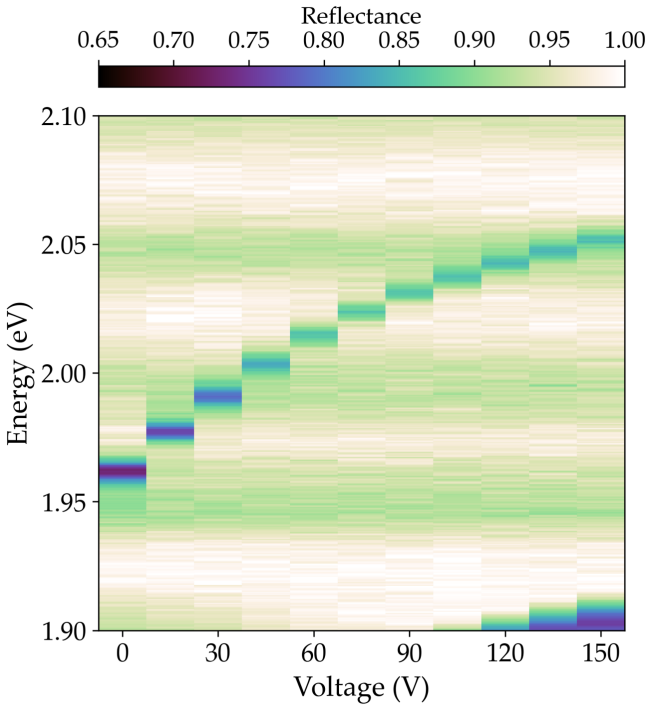

Figure 2.4: **Tunability of the cavity.** Normal incidence reflectance spectra from the cavity for different voltage across the piezo, demonstrates a blue-shift of 90 meV for lower energy cavity mode.

Next, we tested the tunability of another cavity using the piezo. For initial bias of 0V, the two modes appear at 1.962 eV (631.9 nm) and 2.118 eV (585.5 nm) and the reflectance at normal incidence are shown in Fig. 2.4, corresponding to an effective cavity length of 3.98 μm. For 150V, these modes appear at 2.052 eV (604.4 nm) and 2.221 eV (558.1 nm) at normal incidence, indicating a reduced cavity length of 3.64 μm. At this wavelength, this change of 340 nm corresponds to approximately 90 meV of blue-shift (see Fig. 2.4). Note that the change of 340 nm is much smaller than the unloaded specs of the piezo. This is expected since the piezo is pushing against the bottom DBR.

It is important to note that while the exact initial positioning of the modes varies slightly between assembly attempts (for example, Fig. 2.3 and 2.4 represents different assembly attempts), the overall tunability range of about 100 meV remains highly consistent. This re-

liability makes the setup suitable for our experiments to study strong coupling at different detunings.

2.3 Polariton formation

With the successful implementation of a tunable open cavity in the previous section, we then proceed with integrating a monolayer inside the cavity to form exciton polaritons. We prepared a sample by transferring a monolayer WS_2 flake (see Fig. 2.5) onto a DBR substrate using the deterministic dry-transfer method (see section 1.6). WS_2 (sourced from HQGraphene) was chosen for its brightest photoluminescence emission at room temperature compared to other TMDs making it more suitable for testing the cavity. [40, 41]

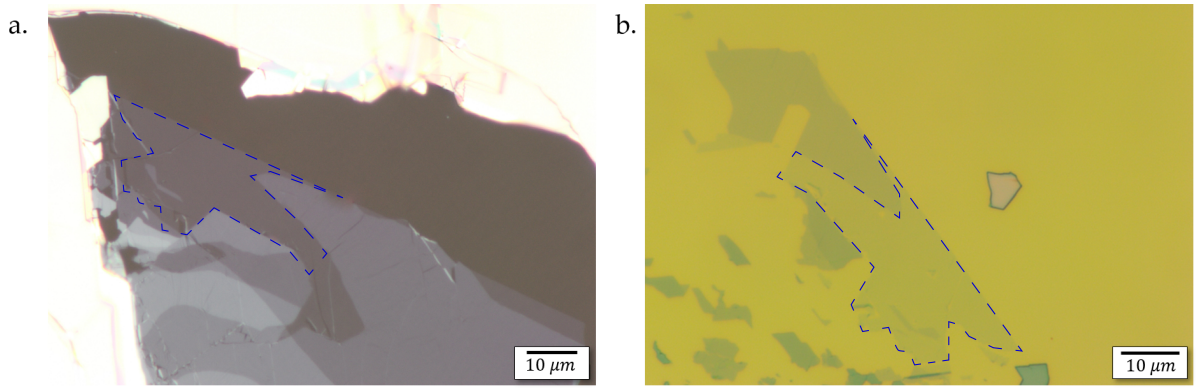

Figure 2.5: **WS_2 monolayer a.** as exfoliated on to a Gel Film, surrounded by few layered and bulk flakes (bright regions). **b.** as transferred onto the DBR substrate. (dashed line indicates the transferred segment of the monolayer on both panels)

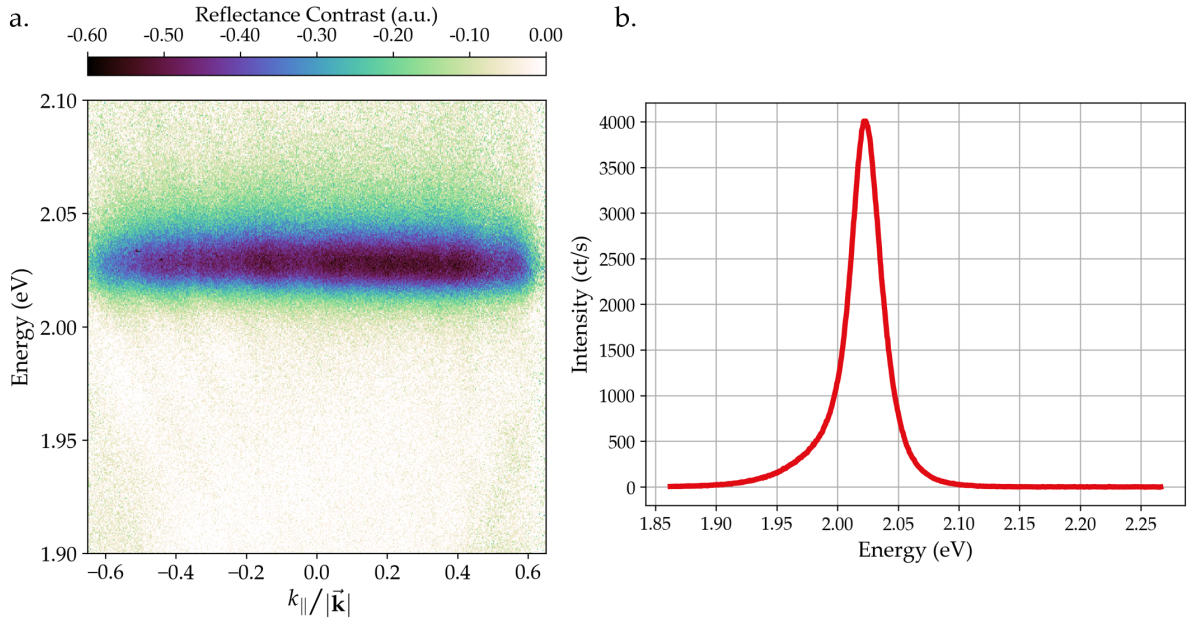

Figure 2.6: **WS_2 monolayer characterization. a.** Angle-resolved reflectance contrast **b.** PL spectrum, showing a strong emission at 2.022 eV

To further characterize this flake, we measured both the reflection contrast and the PL spectrum (see Fig. 2.6). The PL shows a strong emission peak at 2.02 eV which is consistent with reported energy [35] for monolayer WS_2 at room temperature. The strong absorption at similar energies as seen in the reflectance contrast spectra matches with the existing literature [42]. This confirms that flake is indeed a monolayer.

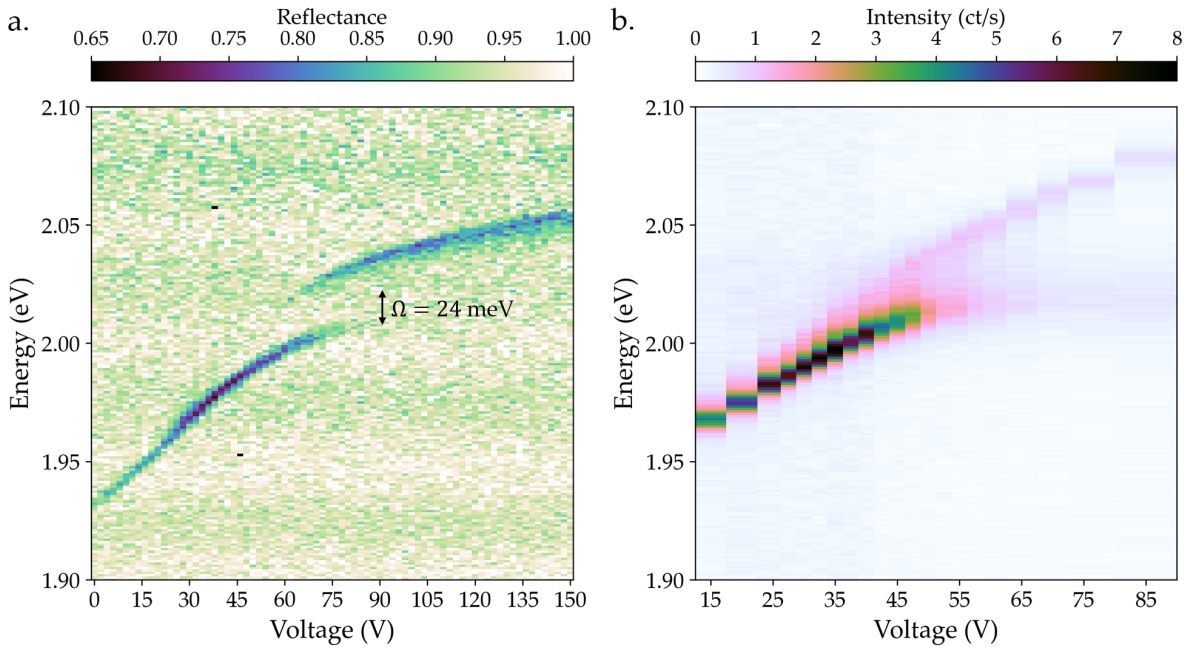

Figure 2.7: **Exciton-polaritons. a.** Normal incidence reflectance spectra from the cavity with WS_2 monolayer as the cavity mode is tuned across the exciton resonance. Anti-crossing behavior with Rabi splitting of about 24 meV. **b.** Normal PL spectra for different voltages across the cavity.

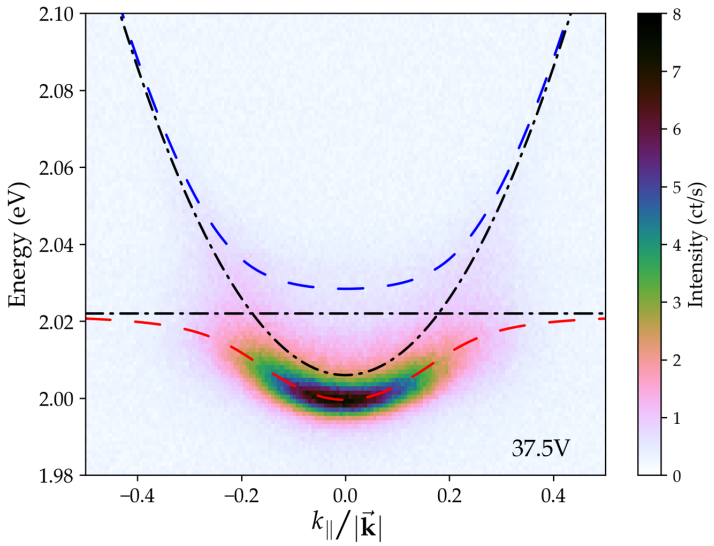

Figure 2.8: **Exciton-polaritons.** Angle-resolved PL spectrum of the cavity. Strong emission from lower polariton (LP). The black lines are the fitted uncoupled cavity mode and exciton resonance. Red line is the LPB and blue line is the upper polariton (UP) branch.

We use this substrate as the bottom DBR for assembling the cavity. In our configuration, the last layer of the DBR has the lower refractive index (SiO_2) to ensure that the field distribution has an antinode for resonant wavelengths at the position of monolayer, maximizing interactions between light and excitons [43]. We then perform measurements on the cavity with integrated monolayer WS_2 for angle-resolved reflectance and PL spectrum while tuning the cavity mode across the exciton resonance.

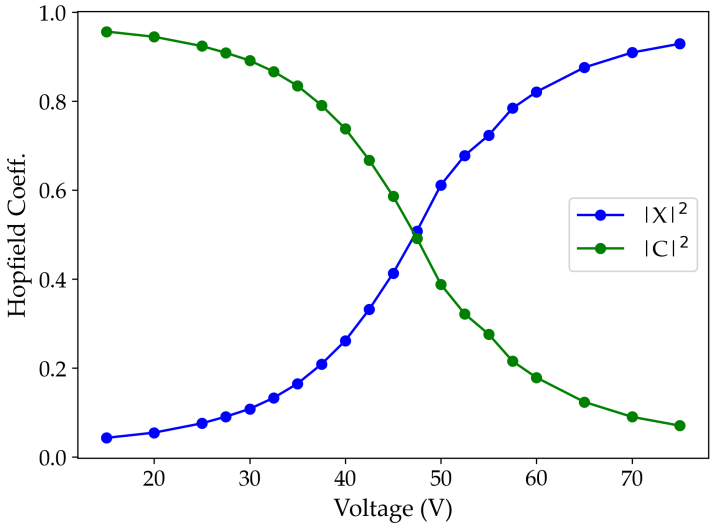

Figure 2.9: **Hopfield coefficients.** Excitonic ($|X|^2$) and photonic ($|C|^2$) fractions for the LP from fitting as the mode is scanned across the resonance.

In figure 2.7a, the reflectance spectra at normal incidence clearly reveals the splitting of the cavity mode as it is tuned across the exciton resonance at 2.02 eV. This characteristic anti-crossing behavior is a definitive signature of strong light-matter coupling, signifying the formation of exciton-polaritons within the cavity. From the observed splitting, we extract a Rabi splitting of $\Omega = 24\ meV$.

Further evidence for strong coupling is provided by the PL spectrum (Fig. 2.7b), which reveals a similar splitting. To quantitatively describe the system, we fit the angle-resolved emission spectra with the theoretical dispersion of the upper and lower branches, treating the detuning between the exciton and cavity mode as a free parameter.
A representative snapshot of the voltage scan at 37.5V across the piezo is shown in Fig. 2.8. For $\Omega = 24\ meV$, the fit yields a detuning of $\Delta E = -16\ meV$ at $k_{||} = 0$ and exciton fraction of $|X|^2 \approx 0.23$ for the lower polariton (LP). Similarly, Fig. 2.9 shows variation in the Hopfield coefficients for LP with voltage across the piezo. This analysis demonstrates a wide tunability (see Fig. 2.10 of the polariton composition within the cavity.

Discussion

In this chapter, I have presented the successful assembly of a tunable open microcavity setup with an integrated WS_2 monolayer. The design ensures minimal degradation of the monolayer's optical properties and control over the exciton-photon detuning. This provides us with a robust and reusable platform for exciton-polaritons in TMDs and further to explore ways of

manipulating their properties.

The next steps will be to (i) integrate bilayers that host interlayer excitons with electrical contacts, and (ii) cool down the sample to demonstrate formation of interlayer exciton polaritons. The next Chapter focuses on part (i).

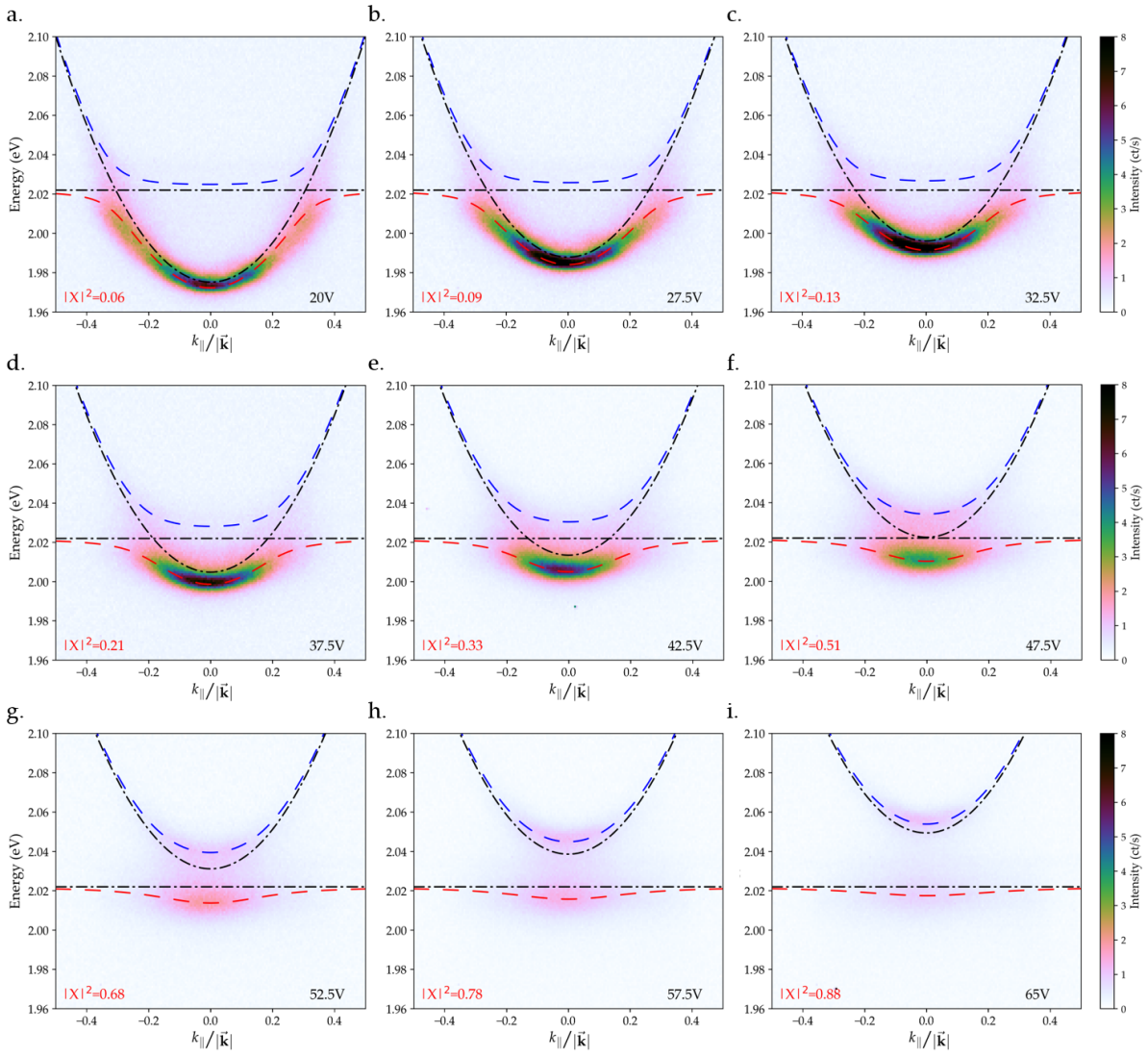

Figure 2.10: **Exciton-polariton.** Angle-resolved PL spectra for different excitonic fractions, along with the fitted UPB (blue) and LPB (red). (a.) corresponds a highly photonic detuning, while (i.) represents a highly excitonic one. (f.) is the one closest to maximum mixing of the exciton with cavity mode.

Chapter 3

Charge Doping and Electric Field Studies

As discussed earlier, TMD monolayers posses a $2\pi/3$ rotational ($\hat{C}_3$) symmetry. In a 2H-homobilayer, this symmetry forbids interlayer hopping for electrons while allowing holes to tunnel between layers [14]. This delocalization of the hole wavefunction across both layers enables hybridization between the B-exciton and the IL-exciton. As a result, the hybridized IL-exciton acquires a substantial oscillator strength while preserving its static out-of-plane dipole moment. In this Chapter, I will present my initial studies on the effects of doping and external electric fields on the excitonic properties especially the IL-exciton.

Among TMDs, MoS_2 exhibits the strongest manifestation of this effect, with the IL-exciton having approximately 36% the oscillator strength of the A-exciton at cryogenic temperatures and it remains visible in absorption spectra even at room temperature [10, 15].

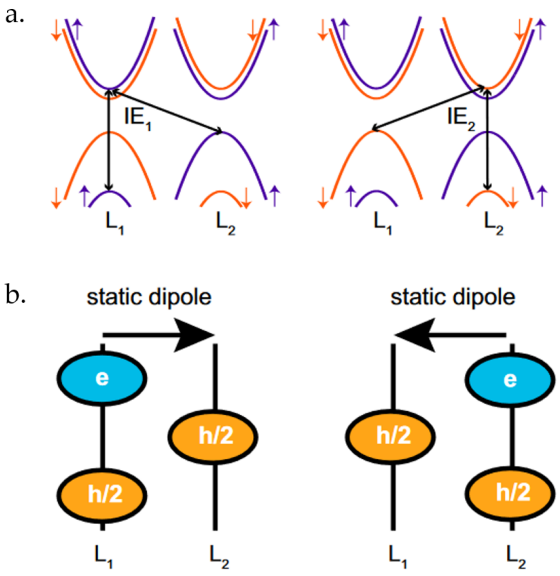

Figure 3.1: **Exciton hybridization. a.** The two possible transition from the higher energy fine splitting of the conduction band are hybridized together. **b.** A schematic diagram showing the delocalisation of the holes and the corresponding direction of the static dipole. Adapted from [10].

3.1 Charge Doping

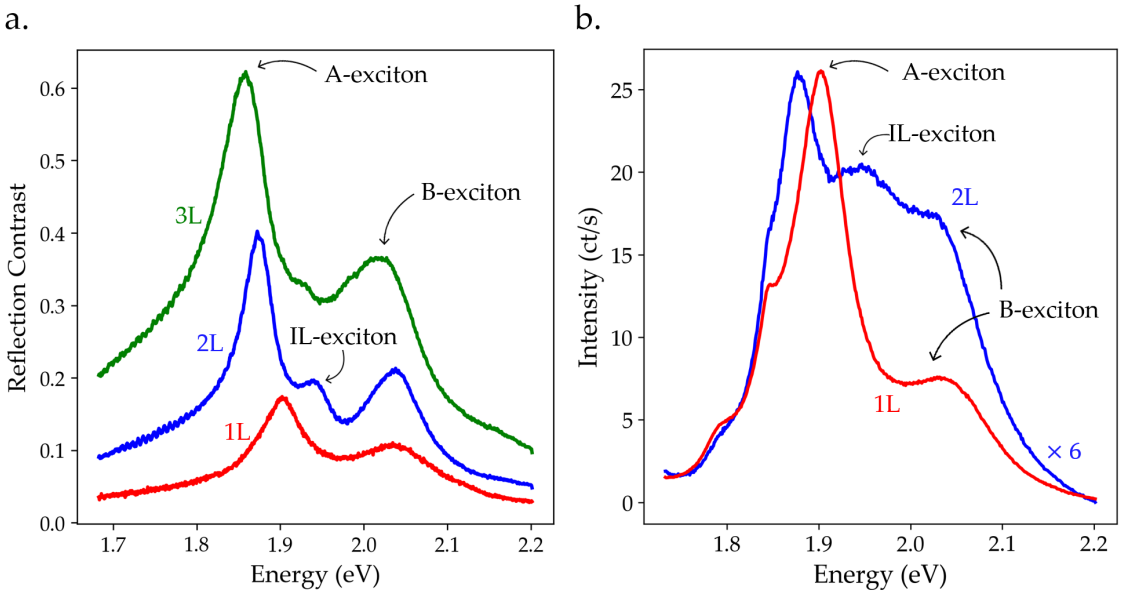

Figure 3.2: **MoS_2 Characterisation. a.** Reflectance Contrast spectrum for mono, bi and trilayer MoS_2. **b.** PL spectrum for mono and bilayer MoS_2.

As discussed in section 1.2, by applying a gate voltage the carrier density in a TMD flake can be tuned. An exfoliated flake is seldom neutral and is naturally doped. Here we tried to use the charge doping to improve the oscillator strength for IL-exciton in bilayer MoS_2.

We first exfoliated MoS_2 onto Gel-film and characterized flakes of varying thickness. Fig. 3.2 presents the measured reflectance contrast and PL spectra for different flakes with different thickness. By comparing these spectra to previous studies [44, 45], we confirmed the layer number of each flake. The A-exciton for the bilayer flake lies at around $\sim 1.875\ eV$ in the reflectance contrast. The B-exciton lies at around $\sim 2.03\ eV$, while the IL-exciton lies at around $\sim 1.945\ eV$. Due to the indirect band gap of the bilayer, PL is significantly weaker compared to the monolayer. The emission remains at similar energies as observed in reflectance contrast.

We then transferred a bilayer onto a n-doped Si/SiO_2 (SiO_2 thickness of 285 nm) substrate with gold contacts patterned on it. The flake was positioned such that a portion of it made direct contact with one of the electrodes (see Fig. 3.3). The substrate was then place on copper tape which is connected to a wire. Furthermore, a connection was made to the top electrode using copper tape, wires and silver paint.

To apply a voltage bias in this configuration (Fig. 3.3b), we utilized the same voltage controller used to drive the piezo in Chapter 2. Fig. 3.4 illustrates the evolution of the reflectance contrast as a function of the applied voltage on the bilayer flake. With increasing voltage, we observe a clear suppression of the A-exciton peak along with a slight redshift. This effect is similar to the observations reported in Ref. [46], where an increase in carrier density leads to an enhancement of the trion peak in the PL spectrum. At room temperature, due to the large linewidths, the exciton and trion peaks cannot be clearly resolved. However, at 83 K, a distinct shift in population from neutral excitons to trions is evident, and a similar mechanism could

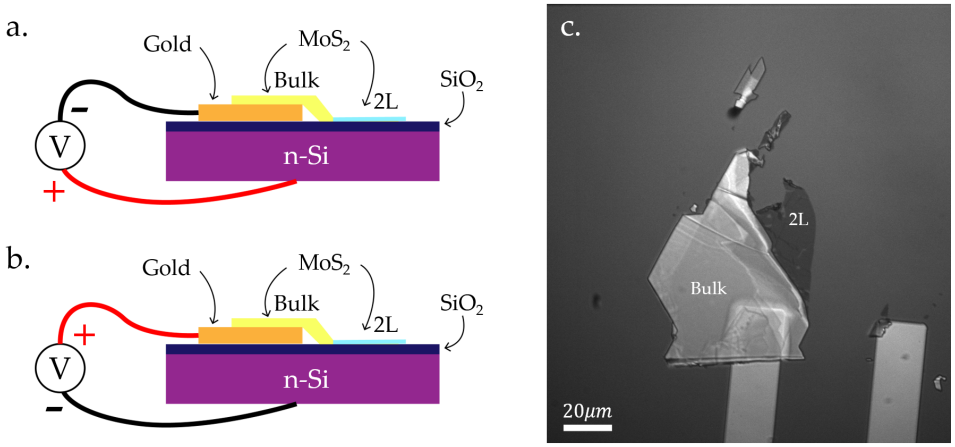

Figure 3.3: **a.** Negative configuration **b.** Positive configuration **c.** Real space image for bilayer MoS_2 transferred on the patterned Si/SiO_2 substrate

be responsible for the suppression and redshift observed here even at room temperature.

The B-exciton peak remains unsuppressed but exhibits a significant redshift, whereas the IL-exciton appears to remain at the same energy. However, the overall energy separation between the IL- and B-exciton gradually decreases with increasing voltage and eventually vanishes at higher voltages. It is important to note that the coupled behaviour of the IL- and B-exciton is due to hybridised nature of these excitonic states. Furthermore, the IL-exciton, which is the primary focus of our investigation, undergoes degradation with increased doping, with no observable improvement at any intermediate voltage.

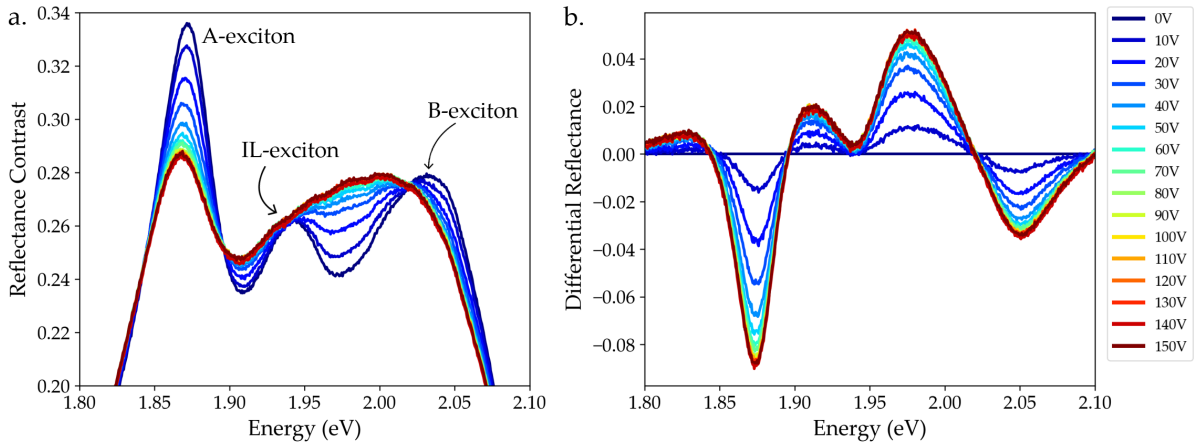

Figure 3.4: **Charge Doping. a.** Reflectance contrast spectrum of MoS2 as the gating voltage is increased. **b.** Differential reflectance $\left(\frac{\Delta R_V}{R_0} = \frac{R_V - R_{V=0}}{R_{V=0}}\right)$ spectrum

We also observe significant hysteresis in the spectrum as the applied voltage is decreased from its maximum value. Fig. 3.5 illustrates the evolution of the reflectance contrast over a complete voltage sweep cycle. In Fig. 3.5a, the voltage is increased from 0V to 150V, corresponding to the changes described earlier, but with individual spectra shown with offsets for clarity. In Fig. 3.5b, the voltage is gradually reduced from 150V back to 0V. Surprisingly, the spectrum regains its original shape, i.e. the spectrum at V=0 before the ramp, around 120V.

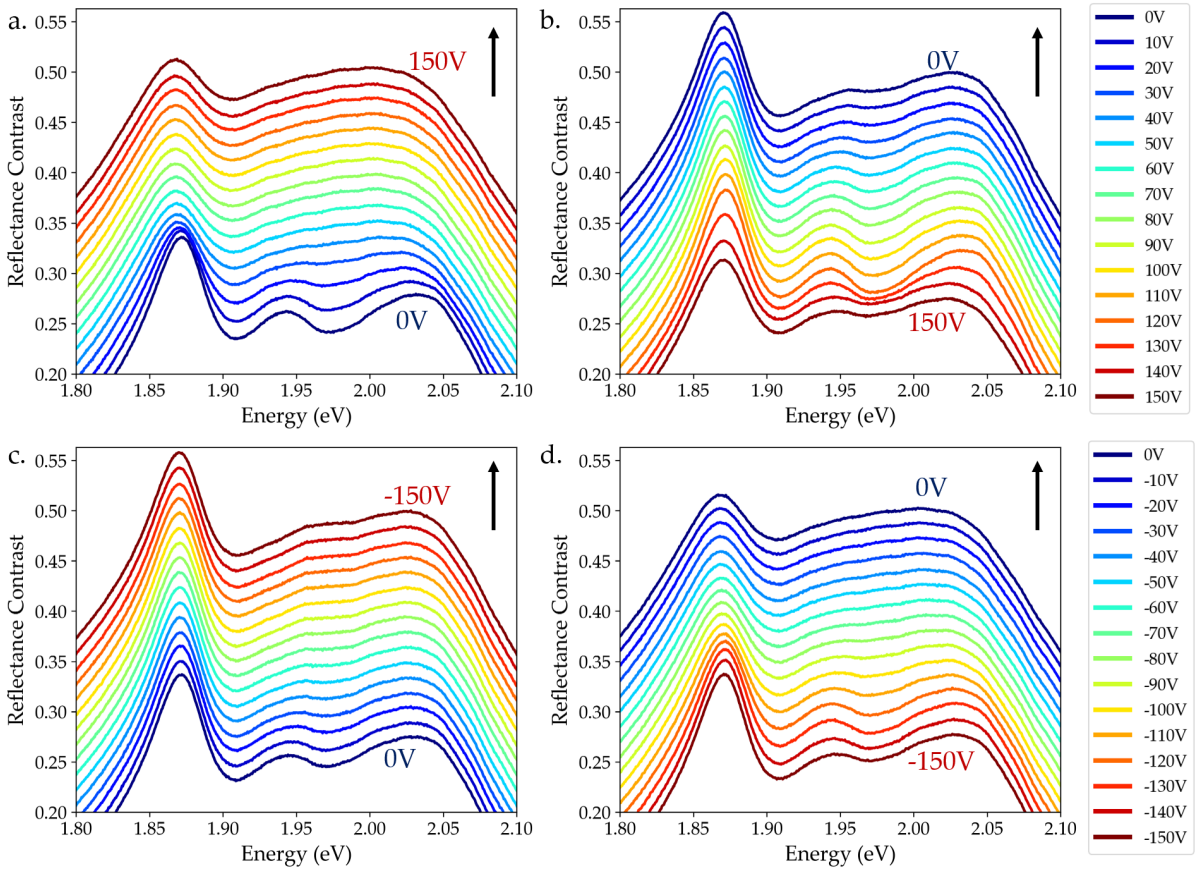

Figure 3.5: **Hysteresis in the spectrum.** Evolution of spectrum as the applied voltage is **a.** increased to 150V in positive configuration. **b.** decreased from 150V in positive configuration. **c.** increased to 150V in negative configuration. **d.** decreased from 150V in negative configuration. Arrows indicate the direction of the voltage ramp.

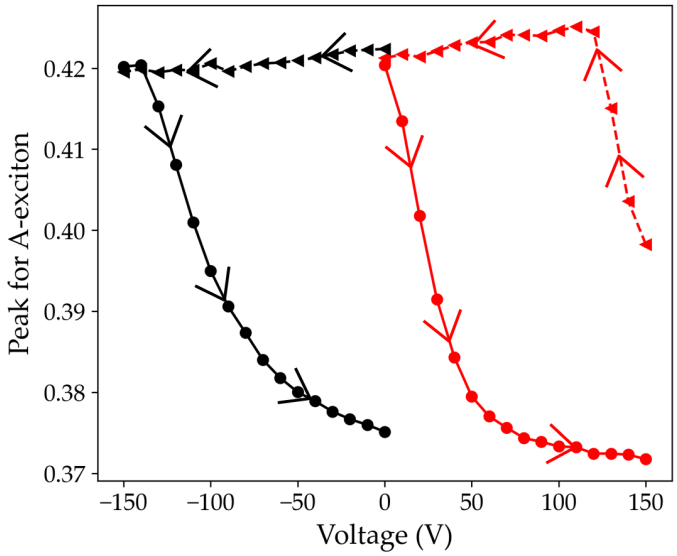

Figure 3.6: **Hysteresis loop.** A voltage sweep for A-exciton's peak height for both positive (red) and negative (black) configuration. The big arrows on the plot shows the direction of voltage step.

Further reduction in voltage does not significantly affect the A-exciton peak height. However, the B-exciton and IL-exciton regions continue to exhibit smooth variations, such that at 0V, this spectral region appears similar to its state at 150V.
To explore the dependence further, we reversed the wiring to apply a negative voltage. In Fig. 3.5c, as the voltage is increased from 0V to -150V, the spectrum remains largely unchanged, except for a slight decrease in the A-exciton peak and broadening of B- and IL- excitons. In Fig. 3.5d, as the voltage is reduced from -150V back to 0V, the A-exciton peak rapidly goes down. Note that this is similar to the behavior observed in Fig. 3.5a, along with the rest of the spectrum.
To quantify the nontrivial behaviour of the spectra as the voltage is ramped up and down, we plot the peak height of the A-exciton, as shown in 3.6. It further highlights the hysteresis in the A-exciton response over the complete voltage cycle.

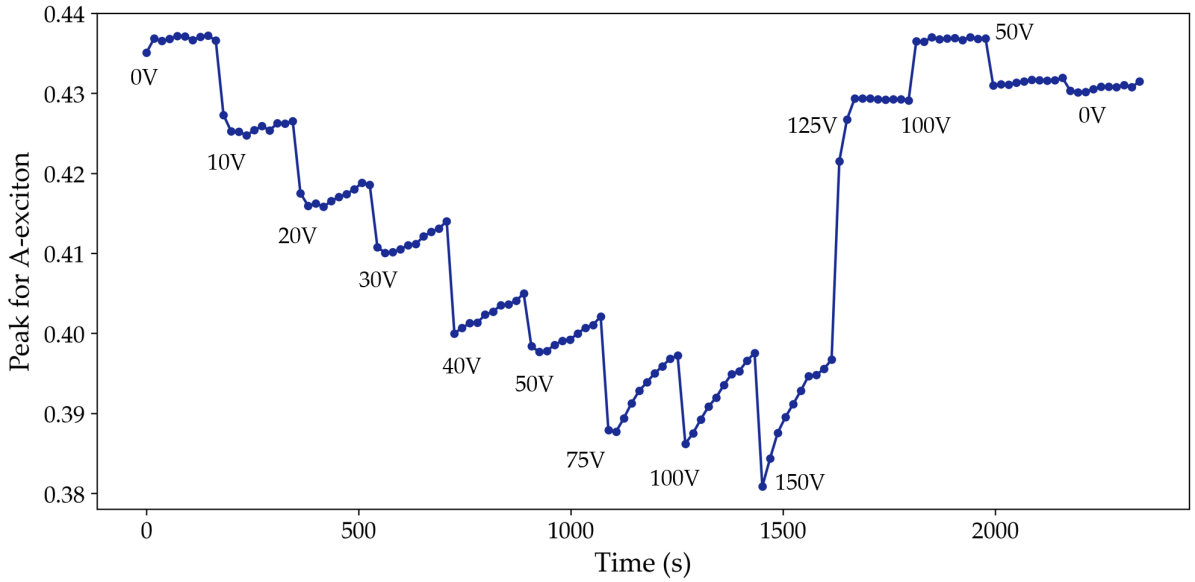

Figure 3.7: **Relaxation in time.** A time series for A-exciton's peak. 10 spectra for each voltages each separated by 18s in time.

These results show that the spectrum is not uniquely determined by the gate voltage, there is a clear dependence on the direction of the ramp. However, it is also important to note that there is also a time dependence. This is obvious from the difference between the spectra at 150 V in Fig. 3.5a,b. Their only difference is the time the spectra were taken. This is the same behaviour for the -150 V in Fig. 3.5c,d. To investigate this behavior further, we performed a time-series measurement, acquiring 10 individual spectra at each voltage, with a time interval of 18 seconds between consecutive spectra. As shown in Fig. 3.7, the spectral features exhibit an initial jump upon changing the voltage, followed by a gradual relaxation over time where the A-exciton intensity increases. However, when the voltage is decreased from 150V to 125V, we observe minimal relaxation after the first few frames. The time-dependent spectra are shown in Fig. 3.8. At 100V, the spectrum fully returns to its original state and remains stable over time, exhibiting no further relaxation. Further decreases in voltage follow a similar trend, with small relaxation, consistent with the behavior observed earlier.

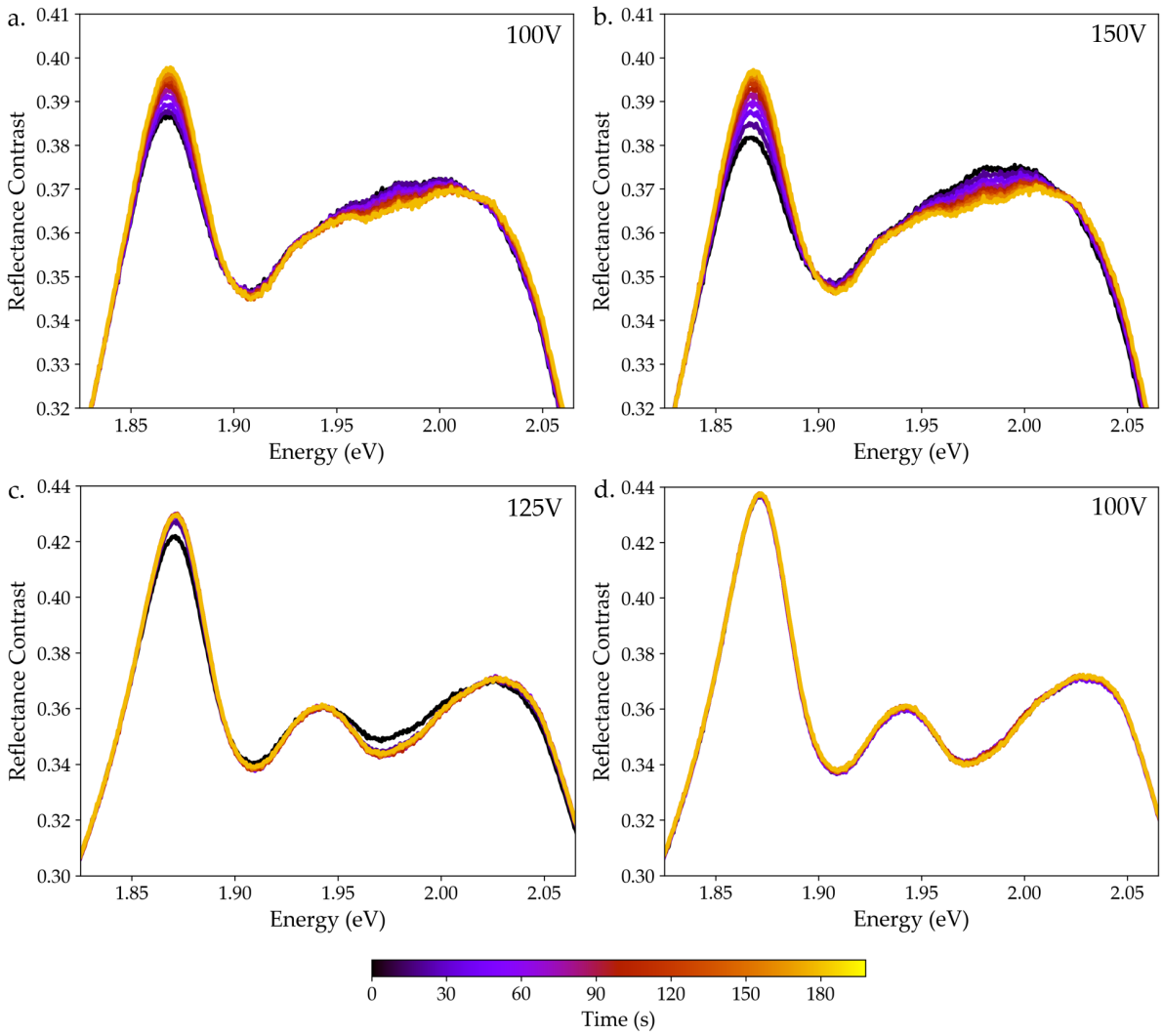

Figure 3.8: **Relaxation in time** Time series for different voltages in positive configuration. **a** and **b** are measured while increasing the voltage, while **c** and **d** are measured with decreasing voltage.

Discussion

The application of gate voltage significantly modifies the optical spectrum of bilayer MoS_2, influencing the behavior of excitonic resonances. As the gate voltage increases, the A-exciton peak is strongly suppressed, while both the interlayer and B-excitons exhibit substantial broadening.

A key observation is the dependence of spectral changes on the direction of voltage sweeping, indicating hysteresis effects. We attribute the observed hysteresis and relaxation in the reflectance spectra to the adsorption of polar molecules from the ambient atmosphere onto the bilayer surface. These adsorbed molecules acts as defects, leading to modifications in the excitonic resonances and overall spectral characteristics. Such effects are commonly observed in atomically thin materials, where surface interactions play a significant role in their properties. [47, 48, 49]

3.2 In-plane Electric Field

As discussed earlier, the IL-exciton possesses a static dipole oriented in the out-of-plane direction, making it highly tunable under an applied electric field. Previous studies have demonstrated this tunability for electric fields perpendicular to the bilayer [8]. In these works, it was shown that this electric field modifies the exciton energy by Stark effect and lifting the degeneracy of static dipole's orientation. However, such a field also tends to align the dipole strictly along the out-of-plane direction, thereby reducing its oscillator strength along the in-plane direction. Hence, we aim to investigate the effects of an in-plane electric field. Since an in-plane field is expected to tilt the dipole more into the plane of the bilayer, it may enhance the exciton's oscillator strength and improve the coupling with the cavity modes.

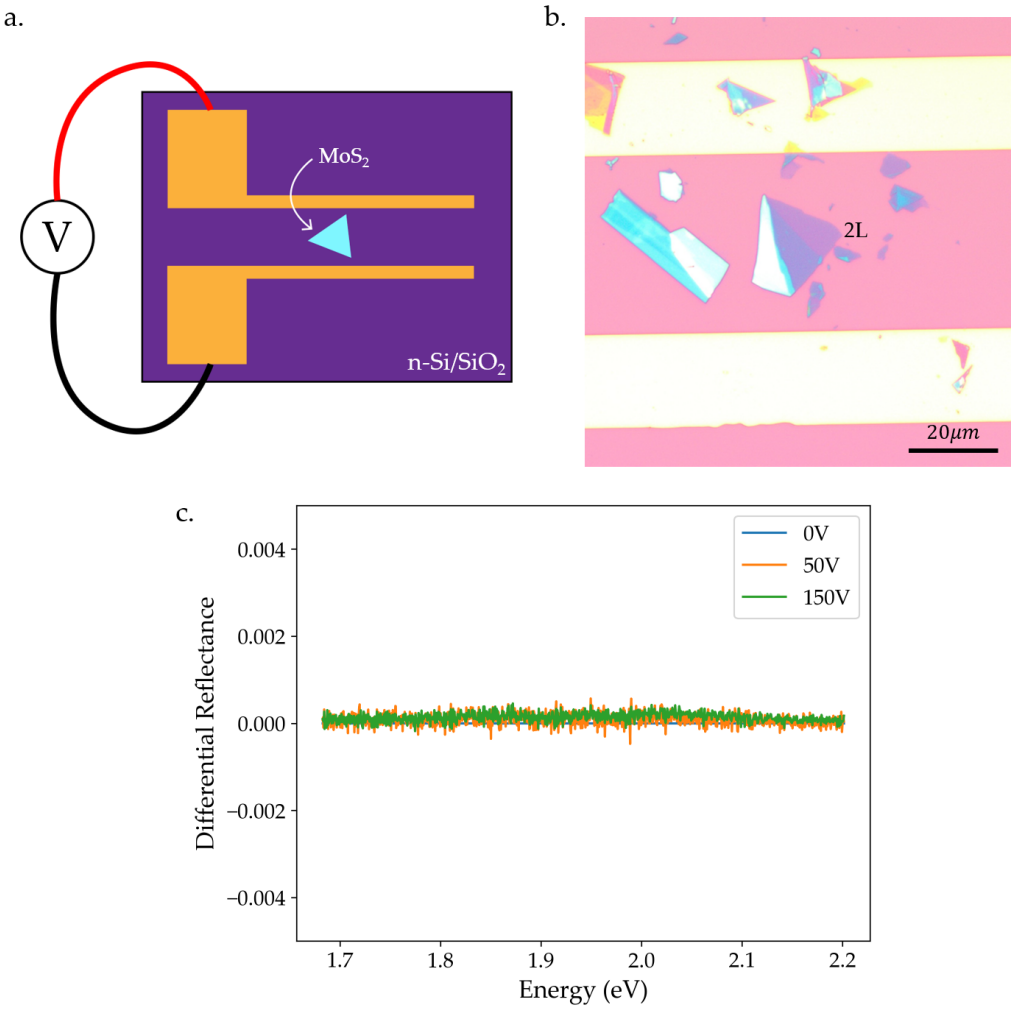

Figure 3.9: **a.** Configuration for in-plane field. **b.** Microscope image of the transferred flake. **c.** Differential reflectance with voltage across the electrodes.

To apply an in-plane electric field to the bilayer, we positioned it between two electrodes using deterministic dry-transfer (see Fig. 3.9a,b). The gold electrodes have a thickness of 50 nm with a separation of about 40 μm. Fig. 3.9 presents a differential reflectance plot illustrating the changes in the spectrum as the applied voltage is increased. However, no significant change beyond the background noise is observed. We attribute this to the presence of electron-rich

substrate, which is relatively close to the electrodes. Any applied in-plane field along the sil-

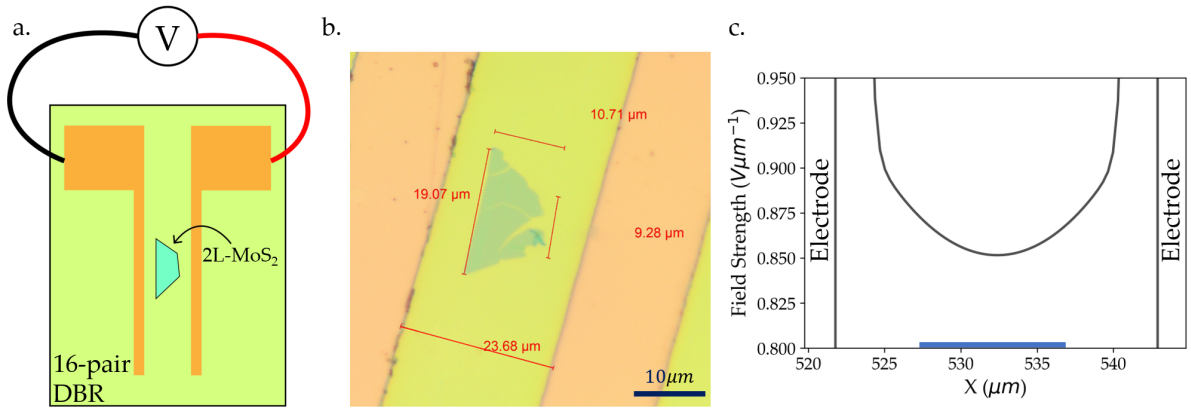

Figure 3.10: **a.** Configuration of the electric field setup on DBR. **b.** Microscope image of the MoS_2 bilayer used for the in-plane field measurements. **c.** Calculated electric field strength between the electrodes at the flakes position. The blue line indicates the approximate extent of flake between electrodes

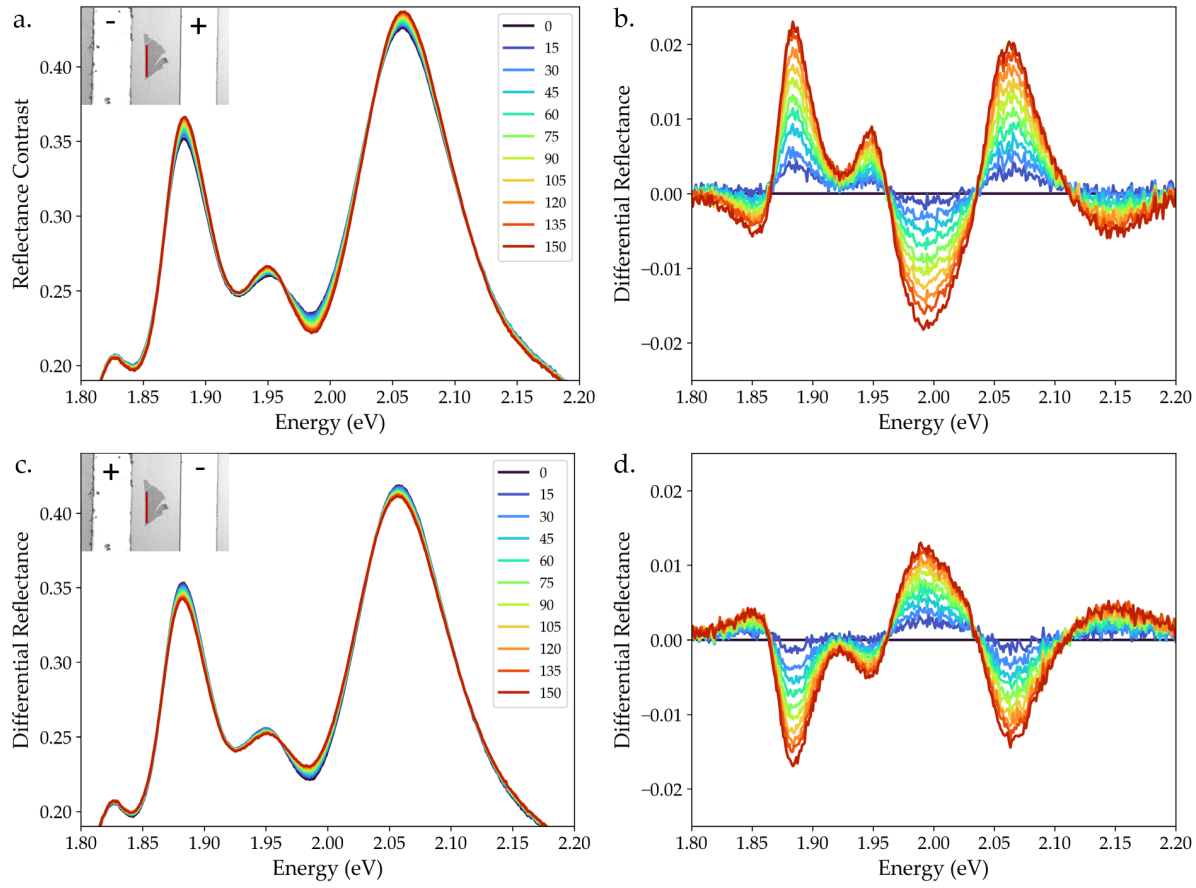

Figure 3.11: **Effect of the in-plane field. a.** Reflectance contrast for field towards left . (Inset shows the polarity). **b.** Differential reflectance for the same polarity as a. **c.** Reflectance contrast for field towards right. (Inset shows the polarity). **d.** Differential reflectance for the same polarity as c.

icon surface likely leads to charge redistribution, effectively screening the electric field and

shielding the bilayer. This suggests that the choice of substrate is not suitable for this experiment. Hence, we moved to an insulating substrate, which is basically our DBR grown on fused silica. Since the ultimate goal of this study is to integrate the system into the open microcavity, we used photolithography to pattern gold electrodes on a 16-pair DBR substrate . The thickness of electrodes is 60 nm. As shown in Fig. 3.10, we placed bilayer MoS_2 flake between the electrodes with a separation of 20μm.

Fig. 3.11a and 3.11c present the reflectance contrast at the straight edge of the bilayer for opposite polarities of the applied voltage (see inset), corresponding to opposite directions of the in-plane electric field. In Fig. 3.11a, as the voltage increases, the peak heights of all three

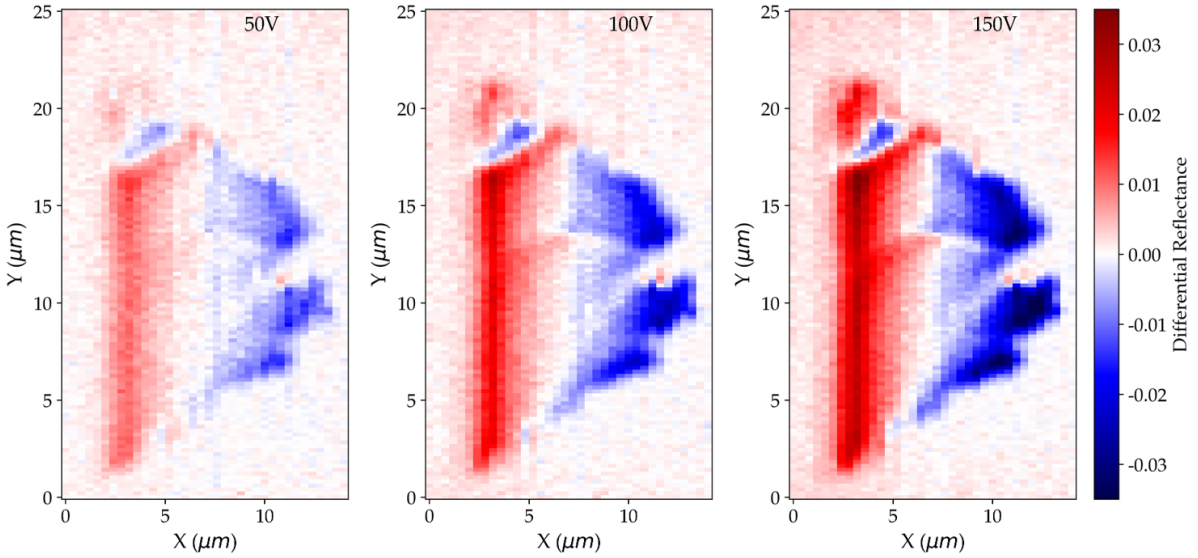

Figure 3.12: Spatially resolved differential reflectance map for A-exciton

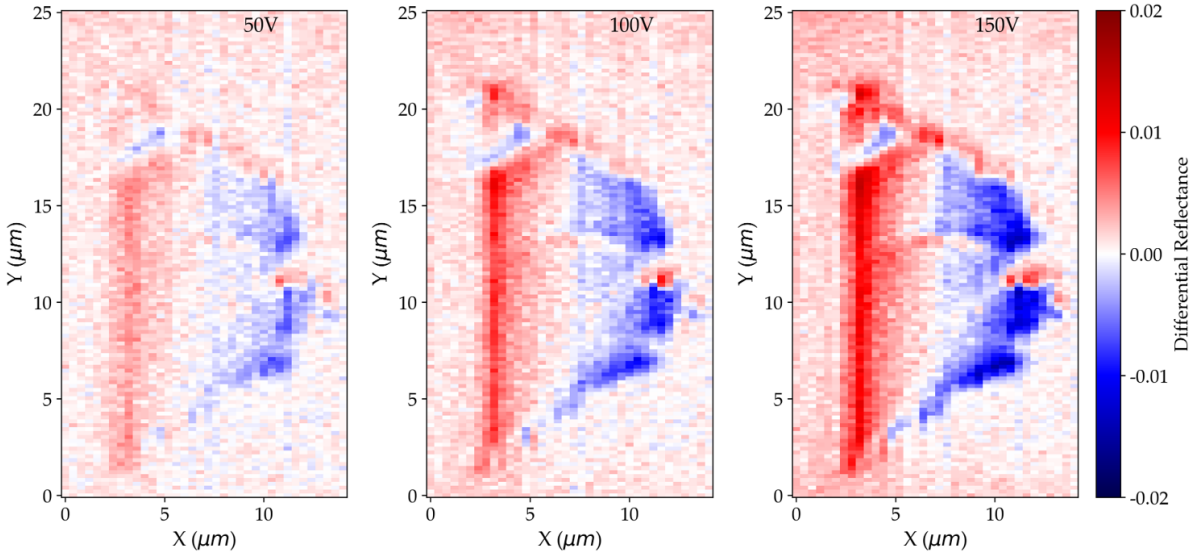

Figure 3.13: Spatially resolved differential reflectance map for IL-exciton

excitons increases, accompanied by a slight decrease in their linewidths. Fig. 3.11c shows the exact opposite effect when the electric field direction is reversed by switching the polarity, with

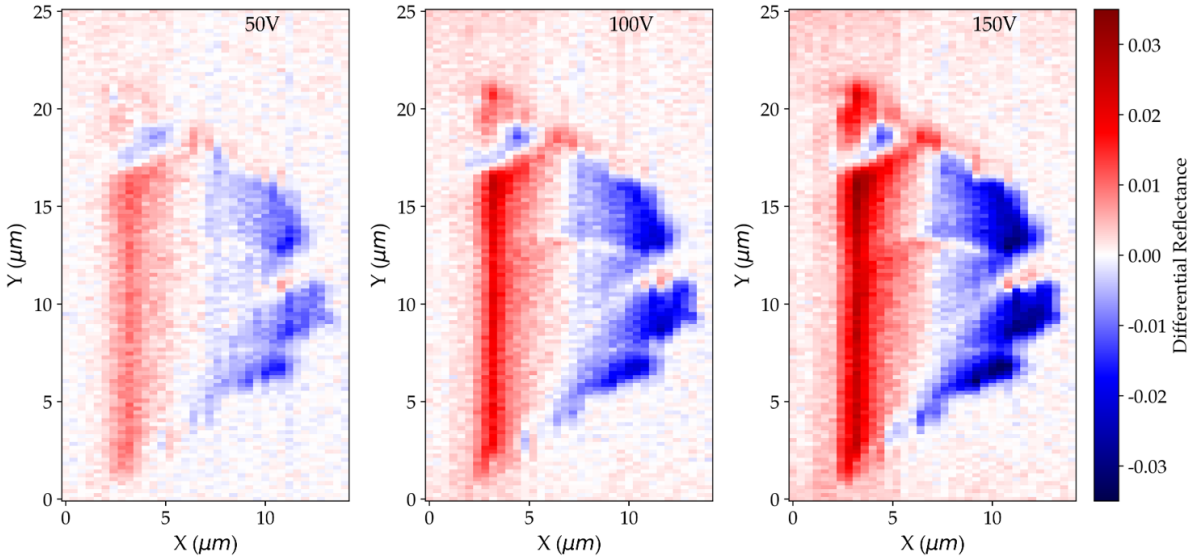

Figure 3.14: Spatially resolved differential reflectance map for B-exciton

a decrease in exciton peak heights and a slight broadening of their linewidths. The differential reflectance plots in Fig. 3.11b and 3.11d provide a clearer visualization of this effect, confirming that the changes in exciton peak heights and linewidths are opposite in nature when the field polarity is reversed. These results shows that the response of the bilayer is reversible and does not show any hysterisis, unlike the gate voltage used in the previous section. Since no additional charge is introduced on the flake in this configuration, any generated field will be of dipole order, which remains extremely weak in the plane perpendicular to the dipole which is the only accessible direction for an adsorbate. Note however, that the spectral changes are very small in comparison to the doping measurements.

During the course of these measurements, we observed that the observed spectral changes varied spatially across the bilayer flake. To systematically investigate this spatial dependence, we utilized the Attocube XY nanopositioner (ECSxy5050/Al/RT) to scan the sample along the X-axis, moving from one edge of the flake to the other across the spectrometer slit. For each X position, we recorded the reflectance spectrum at four different applied voltages: 0V, 50V, 100V, and 150V.

Fig. 3.12 presents the spatially resolved differential reflectance integrated over energies centered around the A-exciton energy. The applied electric field is directed along the positive X-axis. Similarly, Fig. 3.13 and Fig. 3.14 presents the mapping for interlayer and B-exciton, respectively. All three sets of maps clearly shows that one side of the bilayer experiences increased peak intensity while the opposite side experiences the opposite. Consequently, there is a region close to the middle that is unchanged. It is important to note that the top-left corner of the flake is a separate flake of its own and exhibits a similar effect as the entire flake. This suggests that the observed effect depends on the direction of the applied field rather than on any derivative, as would be the case if it were governed by the dielectric polarization of the flake.

Additionally, To quantify the effect of the in-plane electric field on the 3 different in-plane species, we performed multi-peak fitting, and the results are presented in 3.15. The fitting re-

sults show that the A- and B-excitons exhibit a blueshift with increasing electric field, while the ILX remains relatively constant. This behavior is somewhat expected, as theoretical have demonstrated that A and B excitons typically shift together under an applied field [50]. Furthermore, the fitting results indicate that the linewidths of both the IL- and B-exciton narrow with increasing voltage. This suggests a common broadening mechanism for these excitons, which is further supported by the observed increase in their intensity, a trend not seen in the A-exciton.
However, it is important to note that these fitting results do not qualitatively align well with the actual spectra, particularly for the A-exciton. This discrepancy arises due to the presence of a nearby trion peak, which is essential for accurately fitting the spectra. However, because the A-exciton and trion peaks are very close to each other and have broad linewidths, they are not well resolved. This proximity introduces uncertainty in the fitting parameters of both peaks, making the extracted values less reliable. To address this issue, a more reliable approach would be to cool down the sample, which would result in narrower peaks [46] and reduce spectral overlap, thereby improving the accuracy of the analysis.

Discussion

With the application of an in-plane electric field, we have observed a spatially varying modification of the optical response in a bilayer MoS_2.
The next step would be to integrate this system into a microcavity by placing a top mirror on the sample. This would allow us to investigate whether we can control the coupling strength of the IL-exciton to photons. Another way forward is to explore larger electric fields, either by applying higher voltages or reducing the gap between electrodes. Enhancing the field strength could provide deeper insight into the tunability of IL-exciton properties.Ultimately, the goal is to achieve electrical control over the oscillator strength of the IL-exciton and, ideally, to increase it.
A possible explanation for the observed effect is the polaron effect. When an electric field is applied, any free carriers present in a naturally doped bilayer will redistribute. This modification of the Fermi levels could lead to the formation of Fermi polarons in an as-exfoliated bilayer MoS_2 for sufficiently high doping levels. A possible probe into this hypothesis would be to do cryogenic experiments and obtain reliable values for variation in energies and linewidths.

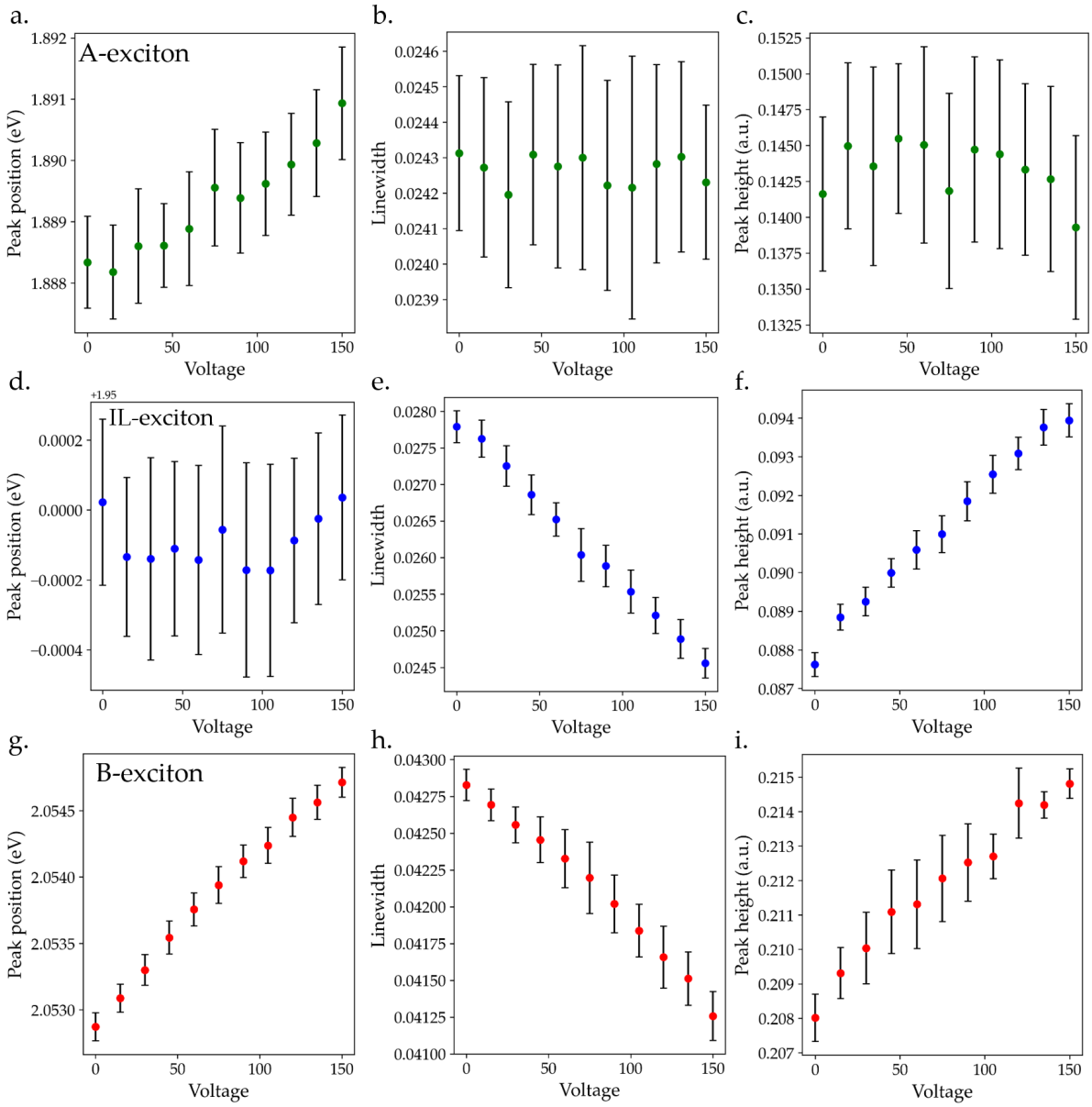

Figure 3.15: Line fitting analysis. Position, linewidth and height of the peak are respectively shown in **a-c** for A-exciton, in **d-f** for IL-exciton and in **g-i** for B-exciton. The error bars are obtained by downsampling 4 datasets each into 12 and then fitting and calculating the mean and standard deviation.

Chapter 4

Conclusion and Outlook

In summary, the work presented in this Thesis demonstrates that we have successfully integrated 2D materials in a open tunable microcavity, and studied the charge doping effects along with in-plane electric field on to these materials. Our findings provide new insights into the tunability of IL-excitons in MoS_2 and their potential for engineering dipolar polariton systems.

Integration of 2D Materials into a Tunable Microcavity

We successfully integrated a monolayer WS_2 into an open and tunable microcavity. Through this platform, we demonstrated strong coupling between excitons and photons, confirming the formation of exciton-polaritons. Additionally, we achieved control over the excitonic and photonic fractions of polaritons by tuning the cavity length. This represents a crucial step toward the realization of dipolar polaritons in bilayer TMD platforms.

Charge Doping Effects in Bilayer MoS_2

We investigated the influence of charge doping on the optical response of homobilayer 2H-MoS_2. Our results show that the spectral response is highly dependent on the direction of voltage sweeping, exhibiting significant hysteresis. However, no noticeable enhancement in the oscillator strength of the IL-exciton was observed, suggesting that charge doping alone may not be an effective method for increasing excitonic coupling in this system.

Tuning IL-Excitons with an In-Plane Electric Field

To explore an alternative method of tuning IL-excitons, we applied an in-plane electric field to bilayer MoS_2. Our measurements reveal a spatially varying optical response, with a small but noticeable improvement in the IL-exciton's oscillator strength. While the effect is modest, it suggests the potential for further exploration. This phenomenon is still under investigation, and we are currently collaborating with theorists to understand its underlying mechanism. The most likely explanation at this stage is the exciton polaron effect, where free carriers interact with excitons under an applied electric field.

Future Directions

The ultimate goal of this research is to advance the realization of polariton-mediated superconductivity by enabling the formation of dipolar polariton Bose-Einstein condensates. This work lays the foundation by demonstrating key methods for controlling IL-excitons, including electrical tuning and cavity integration. The next steps involve integrating electrical contacts within a microcavity platform to achieve precise control over the IL-exciton oscillator strength. Additionally, incorporating the full cavity-electrical control system into a cryostat will allow for low-temperature studies, which are essential for exploring quantum phases and interactions in these systems.

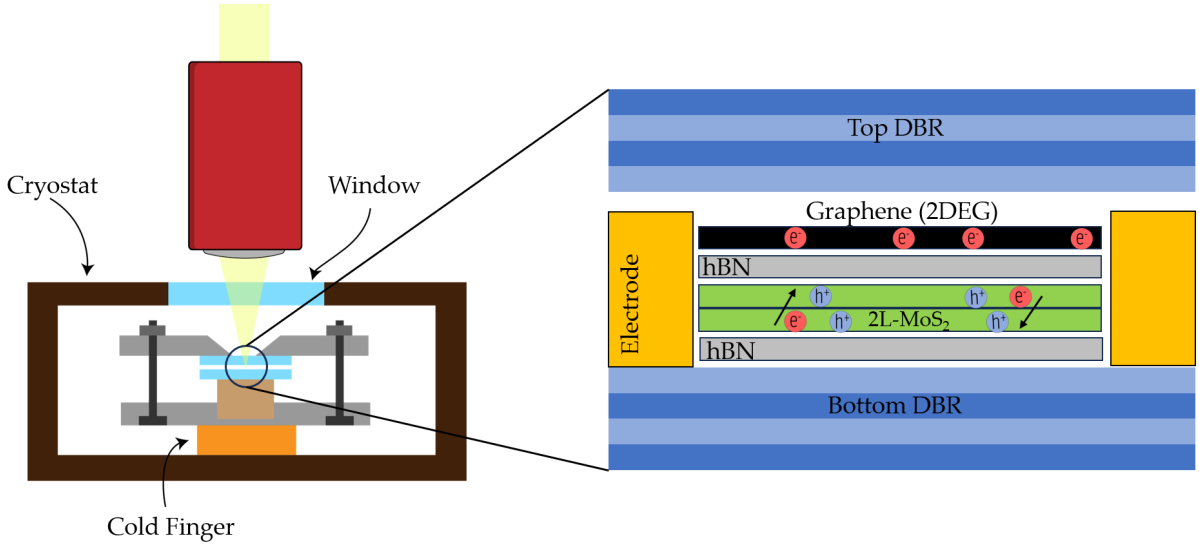

Figure 4.1: **Future plans.** A schematic diagram of the future plans for integrating the cavity into a cryostat and further incorporation of the electrical contacts inside cavity. Ultimately, adding 2DEG and insulating layers for studying the Bose-Fermi interactions.

References

[1] J. Bloch, A. Cavalleri, V. Galitski, M. Hafezi, and A. Rubio, Strongly correlated electron–photon systems, Nature **606**, 41 (2022).

[2] F. P. Laussy, A. V. Kavokin, and I. A. Shelykh, Exciton-Polariton Mediated Superconductivity, Phys. Rev. Lett. **104**, 106402 (2010).

[3] O. Cotleţ, S. Zeytinoğlu, M. Sigrist, E. Demler, and A. Imamoğlu, Superconductivity and other collective phenomena in a hybrid Bose-Fermi mixture formed by a polariton condensate and an electron system in two dimensions, Phys. Rev. B **93**, 054510 (2016).

[4] A. Kuc, N. Zibouche, and T. Heine, Influence of quantum confinement on the electronic structure of the transition metal sulfide T S 2, Phys. Rev. B **83**, 245213 (2011).

[5] T. Cao *et al.*, Valley-selective circular dichroism of monolayer molybdenum disulphide, Nat Commun **3**, 887 (2012).

[6] G. Wang *et al.*, *Colloquium* : Excitons in atomically thin transition metal dichalcogenides, Rev. Mod. Phys. **90**, 021001 (2018).

[7] A. V. Stier, K. M. McCreary, B. T. Jonker, J. Kono, and S. A. Crooker, Exciton diamagnetic shifts and valley Zeeman effects in monolayer WS2 and MoS2 to 65 Tesla, Nat Commun **7**, 10643 (2016).

[8] N. Leisgang *et al.*, Giant Stark splitting of an exciton in bilayer MoS2, Nat. Nanotechnol. **15**, 901 (2020).

[9] D. Thureja *et al.*, Electrically tunable quantum confinement of neutral excitons, Nature **606**, 298 (2022).

[10] B. Datta *et al.*, Highly nonlinear dipolar exciton-polaritons in bilayer MoS2, Nat Commun **13**, 6341 (2022).

[11] M. Matuszewski, T. Taylor, and A. V. Kavokin, Exciton Supersolidity in Hybrid Bose-Fermi Systems, Phys. Rev. Lett. **108**, 060401 (2012).

[12] Z. Huang *et al.*, Spatially indirect intervalley excitons in bilayer WSe2, Phys. Rev. B **105**, L041409 (2022).

[13] A. Zrenner *et al.*, Indirect excitons in coupled quantum well structures, Surface Science **263**, 496 (1992).

[14] P. Rivera *et al.*, Interlayer valley excitons in heterobilayers of transition metal dichalcogenides, Nature Nanotech **13**, 1004 (2018).

[15] I. C. Gerber *et al.*, Interlayer excitons in bilayer MoS 2 with strong oscillator strength up to room temperature, Phys. Rev. B **99**, 035443 (2019).

[16] J. J. Hopfield, Theory of the Contribution of Excitons to the Complex Dielectric Constant of Crystals, Phys. Rev. **112**, 1555 (1958).

[17] J. Kasprzak *et al.*, Bose–Einstein condensation of exciton polaritons, Nature **443**, 409 (2006).

[18] S. Christopoulos *et al.*, Room-Temperature Polariton Lasing in Semiconductor Microcavities, Phys. Rev. Lett. **98**, 126405 (2007).

[19] J. Frenkel, On the Transformation of light into Heat in Solids. I, Phys. Rev. **37**, 17 (1931).

[20] H. Deng, H. Haug, and Y. Yamamoto, Exciton-polariton Bose-Einstein condensation, Rev. Mod. Phys. **82**, 1489 (2010).

[21] A. Perot and C. Fabry, On the Application of Interference Phenomena to the Solution of Various Problems of Spectroscopy and Metrology, ApJ **9**, 87 (1899).

[22] A. K. Geim and I. V. Grigorieva, Van der Waals heterostructures, Nature **499**, 419 (2013).

[23] K. F. Mak, C. Lee, J. Hone, J. Shan, and T. F. Heinz, Atomically Thin MoS 2 : A New Direct-Gap Semiconductor, Phys. Rev. Lett. **105**, 136805 (2010).

[24] A. Chernikov *et al.*, Exciton Binding Energy and Nonhydrogenic Rydberg Series in Monolayer WS 2, Phys. Rev. Lett. **113**, 076802 (2014).

[25] M. M. Ugeda *et al.*, Giant bandgap renormalization and excitonic effects in a monolayer transition metal dichalcogenide semiconductor, Nature Mater **13**, 1091 (2014).

[26] C. Schneider *et al.*, Exciton-polariton trapping and potential landscape engineering, Rep. Prog. Phys. **80**, 016503 (2017).

[27] M. Palummo, M. Bernardi, and J. C. Grossman, Exciton Radiative Lifetimes in Two-Dimensional Transition Metal Dichalcogenides, Nano Lett. **15**, 2794 (2015).

[28] G. Moody *et al.*, Intrinsic homogeneous linewidth and broadening mechanisms of excitons in monolayer transition metal dichalcogenides, Nat Commun **6**, 8315 (2015).

[29] H. Wang *et al.*, Radiative lifetimes of excitons and trions in monolayers of the metal dichalcogenide MoS 2, Phys. Rev. B **93**, 045407 (2016).

[30] A. Raja *et al.*, Coulomb engineering of the bandgap and excitons in two-dimensional materials, Nat Commun **8**, 15251 (2017).

[31] K. F. Mak *et al.*, Tightly bound trions in monolayer MoS2, Nature Mater **12**, 207 (2013).

[32] E. Courtade *et al.*, Charged excitons in monolayer WSe 2 : Experiment and theory, Phys. Rev. B **96**, 085302 (2017).

[33] B. Ganchev, N. Drummond, I. Aleiner, and V. Fal'ko, Three-Particle Complexes in Two-Dimensional Semiconductors, Phys. Rev. Lett. **114**, 107401 (2015).

[34] F. Katsch and A. Knorr, Doping-induced non-Markovian interference causes excitonic linewidth broadening in monolayer WSe2, Phys. Rev. B **105**, L041401 (2022).

[35] B. Zhu, X. Chen, and X. Cui, Exciton Binding Energy of Monolayer WS2, Sci Rep **5**, 9218 (2015).

[36] J. B. Muir *et al.*, Interactions between Fermi polarons in monolayer WS2, Nat Commun **13**, 6164 (2022).

[37] K. S. Novoselov *et al.*, Electric Field Effect in Atomically Thin Carbon Films, Science **306**, 666 (2004).

[38] T. Yun *et al.*, Influence of direct deposition of dielectric materials on the optical response of monolayer WS2, Applied Physics Letters **119**, 133106 (2021).

[39] D. Babic and S. Corzine, Analytic expressions for the reflection delay, penetration depth, and absorptance of quarter-wave dielectric mirrors, IEEE J. Quantum Electron. **28**, 514 (1992).

[40] K. M. McCreary, A. T. Hanbicki, S. V. Sivaram, and B. T. Jonker, A- and B-exciton photoluminescence intensity ratio as a measure of sample quality for transition metal dichalcogenide monolayers, APL Materials **6**, 111106 (2018).

[41] L. C. Flatten *et al.*, Room-temperature exciton-polaritons with two-dimensional WS2, Sci Rep **6**, 33134 (2016).

[42] A. Hanbicki *et al.*, Anomalous temperature-dependent spin-valley polarization in monolayer WS2, Sci Rep **6**, 18885 (2016).

[43] F. Barachati *et al.*, Interacting polariton fluids in a monolayer of tungsten disulfide, Nature Nanotech **13**, 906 (2018).

[44] F. Carrascoso, D.-Y. Lin, R. Frisenda, and A. Castellanos-Gomez, Biaxial strain tuning of interlayer excitons in bilayer MoS $_2$, J. Phys. Mater. **3**, 015003 (2020).

[45] I. Neri, M. López-Suárez, S. Caponi, and M. Mattarelli, Fast MoS$$_2$$ thickness identification by transmission imaging, Appl Nanosci **11**, 605 (2021).

[46] J. Pei *et al.*, Exciton and Trion Dynamics in Bilayer MoS $_2$, Small **11**, 6384 (2015).

[47] D. J. Late, B. Liu, H. S. S. R. Matte, V. P. Dravid, and C. N. R. Rao, Hysteresis in Single-Layer MoS_2 Field Effect Transistors, ACS Nano **6**, 5635 (2012).

[48] A. Di Bartolomeo *et al.*, Hysteresis in the transfer characteristics of MoS_2 transistors, 2D Mater. **5**, 015014 (2017).

[49] T. Knobloch *et al.*, A Physical Model for the Hysteresis in MoS_2 Transistors, IEEE J. Electron Devices Soc. **6**, 972 (2018).

[50] B. Scharf *et al.*, Excitonic Stark effect in MoS 2 monolayers, Phys. Rev. B **94**, 245434 (2016).